



Julian Eiperle

Dependence of the scrape-off layer electron temperature decay length on the toroidal magnetic field and plasma current in the ASDEX Upgrade tokamak

IPP 2024-22
August 2024



universität
uulm

**Fakultät für
Naturwissenschaften**
IPP Garching

Dependence of the scrape-off layer electron temperature decay length on the toroidal magnetic field and plasma current in the ASDEX Upgrade tokamak

Abschlussarbeit an der Universität Ulm

Vorgelegt von:

Julian Eiperle
Julian.Eiperle@uni-ulm.de
1052296

Gutachter:

apl. Prof. Dr. Emanuele Poli

Betreuer:

Dr. Davide Silvagni

2022

Version June 7, 2022

© 2022 Julian Eiperle

Satz: PDF- \LaTeX 2 ϵ

Contents

1	Introduction	1
2	The principle of a tokamak	3
2.1	The magnetic fields in a tokamak	3
2.2	The scrape-off layer	4
2.3	L-mode and H-mode	6
2.4	Edge-localized modes (ELMs)	8
3	Scrape-off layer physics	10
3.1	Parallel heat flux	10
3.2	Calculating $T(s_{ })$	11
3.3	Theoretical dependencies of λ_{Te}	15
4	Methodology	19
4.1	The Thomson Scattering system in ASDEX-Upgrade	19
4.2	Calculation of the decay lengths λ_{Te} and λ_n	21
4.3	Impact of the radial interval on the decay lengths	26
5	Results	28
5.1	Database description	28
5.2	Scrape-off layer decay lengths	31
5.3	λ_{Te} trends at constant I_p	38
5.4	λ_{Te} trends at constant q_{95}	43
6	Conclusion	46
	Bibliography	48

1 Introduction

One of the biggest challenges of our time is to deal with the climate change. Humanity has to reduce CO₂ emissions in order to keep the living conditions on earth bearable for future generations.

This sets lots of new tasks for the society, regarding mobility, heating, industry and electricity production. Regarding the latter, the production of electricity without emitting greenhouse gases can be obtained with like hydro power, wind and solar energy. However, for a hydroelectric power plant one needs certain conditions on the location and solar and wind energy are depending on the weather conditions.

Another way to produce electricity without emitting CO₂ is by nuclear power plants. Nuclear energy production does not depend on the weather conditions and produces lots of energy for the small area needed. However, the major problems of this technology are nuclear waste and safety issues.

There are two ways to generate energy from a nuclear power plant. The first is fission. In nuclear fission, massive nuclei, like uranium, release binding energy, when they are divided in two lighter elements, which have a mass closer to an iron nucleus. This is because the element with the highest binding energy per nucleon is iron. The second way to generate energy from a nuclear power plant is by nuclear fusion. In nuclear fusion, two nuclei, lighter than iron are combined and produce a heavier element, with a mass closer to iron and higher binding energy, which is released during the process. The sun uses protons for this process, but the highest fusion probability for the lowest temperature is achieved with a deuterium-tritium fusion, so that is the most promising fuel for future fusion plants.

While humanity has not yet managed to gain energy through a fusion plant, all the energy we use is still coming out of nuclear fusion, because that is the way the sun is producing energy. For a self-perpetuating fusion process the so called triple product [1] $nT\tau$ has to exceed a certain value. Here T is the temperature and n the

particle density of the ions in the plasma and τ the energy confinement time, which describes the time in which the plasma loses its energy [2]. The sun reaches this ignition condition through a high density in its core.

However, one cannot reach such high particle densities on Earth, therefore the triple product is increased by rising the temperature. On Earth the temperature needs to be around 150 million K, which is ten times higher than the Sun's core.

The most promising way to reach such high temperature is the tokamak, which keeps the fuel in a torus-shaped vacuum chamber through magnetic confinement. At this high temperatures, the fuel is in the status of plasma. In this thesis, temperature and density profiles of the mid-sized ASDEX-Upgrade tokamak, located in Garching, will be analysed, in order to determine the dependencies of the decay lengths in the plasma edge region. Those are important for future fusion power plants, because they correlate with the heat flux on the wall components and therefore determine their abrasion.

2 The principle of a tokamak

2.1 The magnetic fields in a tokamak

One of the most promising concept for a future fusion device is the tokamak. In a tokamak there are toroidal field coils, which create a toroidal magnetic field B_{tor} and there is a plasma current I_p flowing in the toroidal direction, which creates a poloidal magnetic field B_{pol} [3]. The resulting magnetic field B is helical. These magnetic fields are shown in fig. 2.1.

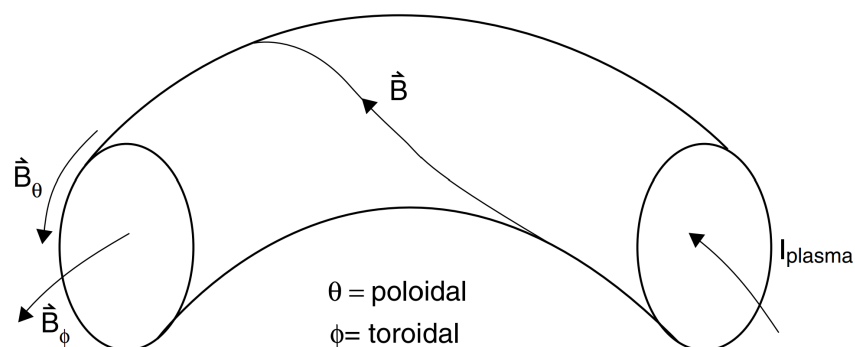


Figure 2.1: The magnetic fields of a tokamak. Here B_ϕ is the toroidal magnetic field, created by field coils and B_θ is the poloidal magnetic fields, resulting from the plasma current.[3]

This resulting field B forms closed surfaces around the plasma core. Since charged particles move along magnetic field lines due to Lorentz force, this magnetic field configuration will confine the plasma in the tokamak.

2.2 The scrape-off layer

Fig. 2.2 shows a poloidal cross section of a tokamak. Two kinds of magnetic field lines can be distinguished: "closed" magnetic field lines lay on fully closed magnetic flux surfaces and magnetic field lines, that intercept a solid surface, called "open" [3]. The *last closed flux surface* (LCFS), does not touch a solid surface. It separates the plasma in two regions: The confined region inside of it and the scrape-off layer (SOL) outside, where the magnetic field lines are in contact with the wall [1].

It is convenient to introduce the normalized minor plasma radius ρ_{pol} [1]:

$$\rho_{\text{pol}} = \sqrt{\frac{\Psi - \Psi_{\text{axis}}}{\Psi_{\text{LCFS}} - \Psi_{\text{axis}}}}, \quad (2.1)$$

where Ψ is the poloidal magnetic flux, Ψ_{LCFS} is the flux at the LCFS and Ψ_{axis} is the flux through the ring defined by the magnetic axis [1]. According to this definition one can characterize the confined region by $\rho_{\text{pol}} < 1$ and the SOL by $\rho_{\text{pol}} > 1$.

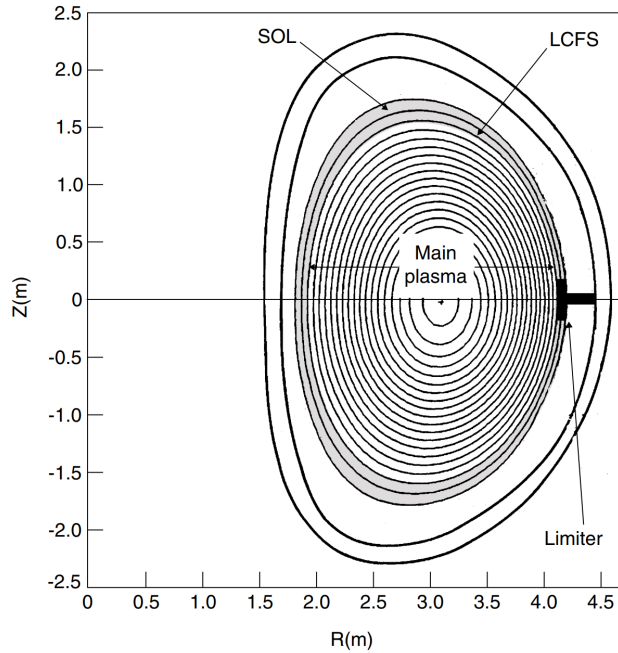


Figure 2.2: The magnetic flux surfaces shown in a cross section through the poloidal plane in a JET-sized tokamak. The LCFS is the last closed flux surface, limited by the limiter.[3]

To describe the twisting of a magnetic field line, one defines the safety factor:

$$q_s = \frac{r B_{\text{tor}}}{R B_{\text{pol}}} \quad (2.2)$$

Here r is the minor radius of the magnetic flux surface and R is the major radius. The safety factor determines the number of turns of the field line in poloidal direction, while going around in toroidal direction [2]. The safety factor as written in eq. (2.2) is only an approximation for tokamaks with large aspect ratio $A = \frac{R}{a}$, with a as the minor plasma radius [1]. This is a good approximation for typical tokamaks [1]. In the experimental part of this thesis q_s is taken at $\rho_{\text{pol}} = 0.95$ and it will be called q_{95} . The reason for this is that B_{pol} is 0 at the LCFS, so q_s diverges.

Another important concept shown in fig. 2.2 and fig. 2.3(a) is the *limiter*. This protruding element is introduced to prevent the plasma particles, that enter the SOL, from hitting the tokamak's wall, which causes erosion [1]. However the problem of the limiter configuration is that it introduces large amounts of impurities to the plasma, which are atoms other than deuterium and tritium, by sputtering of the wall materials, desorption of surface atoms, arcing, evaporation of bulk material, and chemical reactions [1]. The introduced impurities cause increased radiation losses and fuel dilution, which lead to a reduced plasma core pressure and therefore less fusion reactions [1].

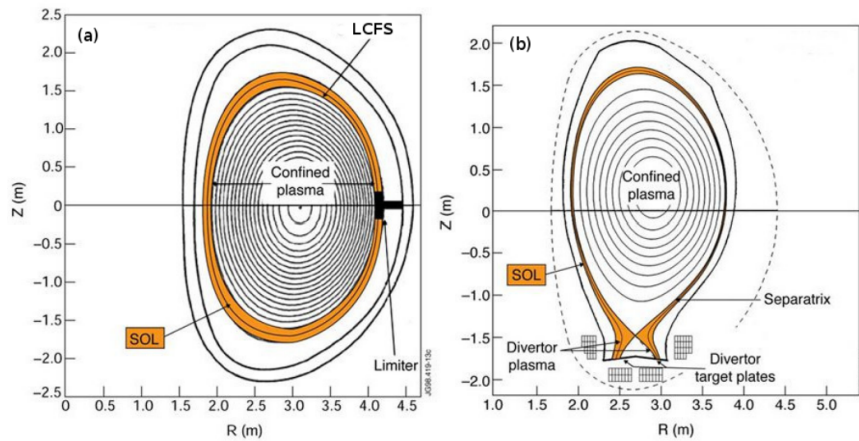


Figure 2.3: A limiter (a) and divertor (b) configuration for JET [1].

To solve this problem and still keep the plasma away from the wall, the *Divertor* configuration was introduced. In this configuration additional field coils carry a current

parallel to I_p in toroidal direction, which causes a point where the poloidal magnetic field vanishes, called the X-point [1]. The X-point can be created in the lower or upper part of the vessel, an example of a divertor plasma with X-point in the lower part of the vessel is shown in fig. 2.3(b). The magnetic flux surface that passes the X-point is termed the separatrix [1]. Another important component of the divertor configuration are the divertor target plates [1]. All plasma particles that enter the SOL will move along the magnetic field lines and hit the divertor target plates. Since those parts of the tokamak are in direct contact with the plasma, they need to stand very high temperatures, which is why they are made out of tungsten. The divertor configuration has many advantages compared to the limiter one, e.g. reduced impurity in the confined plasma, better helium pumping and reaching higher energy confinement regimes [1]. Those confinement regimes will be the topic of the next section.

2.3 L-mode and H-mode

The confinement regimes in tokamaks with divertor configuration can be divided in two main categories: The low-energy confinement mode (L-mode) and the high-energy confinement mode (H-mode) [1].

As shown in fig. 2.4, the L-mode is characterised by a shallower electron edge temperature and density gradient than the H-mode and a lower energy confinement time τ than the H-mode [1]. The H-mode brings a strong turbulence suppression, caused by the so-called edge transport barrier in plasma temperature and density, resulting in a pedestal at the plasma edge (as shown in fig. 2.4) [2]. Tokamaks with divertor configuration can easily achieve H-mode, which is the reason why it was only discovered in 1982, in the first diverted tokamak (ASDEX) [1].

Since the H-mode reaches approximately twice the edge electron density and temperature as the L-mode, it's the more promising regime for future fusion devices [2].

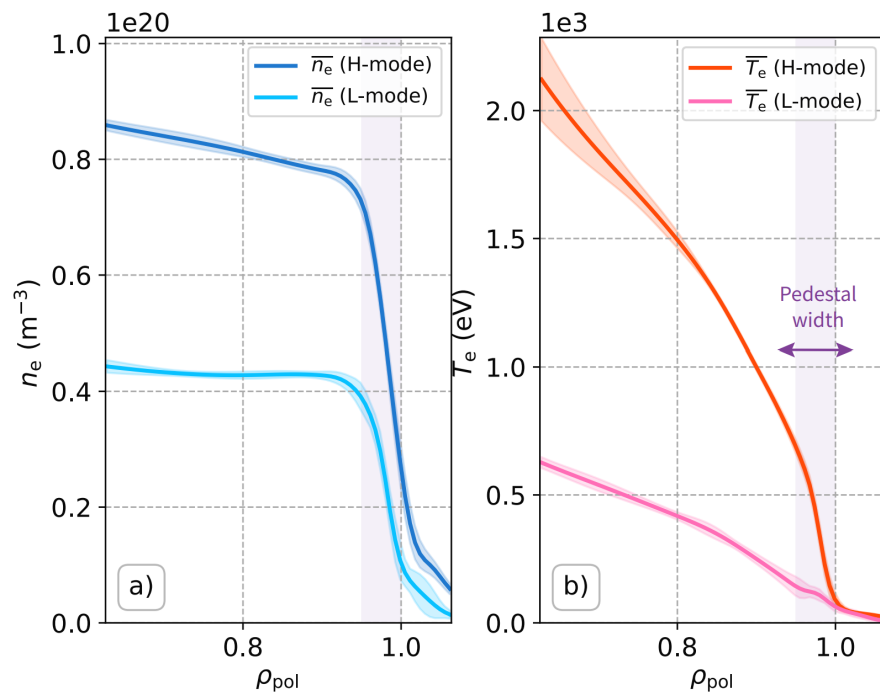


Figure 2.4: The high confinement regime (darker colors) compared to the low confinement regime (brighter colors). The electron density (a) and electron temperature (b) are plotted against the normalized plasma radius ρ_{pol} [2]

2.4 Edge-localized modes (ELMs)

In H-Mode the high pressure gradient at the edge leads to plasma instabilities, termed "Edge-localized Modes", or short *ELMs* [4]. ELMs are periodically appearing magnetohydrodynamic instabilities [1], which crash the pedestal in fig. 2.4 in H-mode and flush out energy and particles from the plasma to the Tokamak's wall and divertor [4].

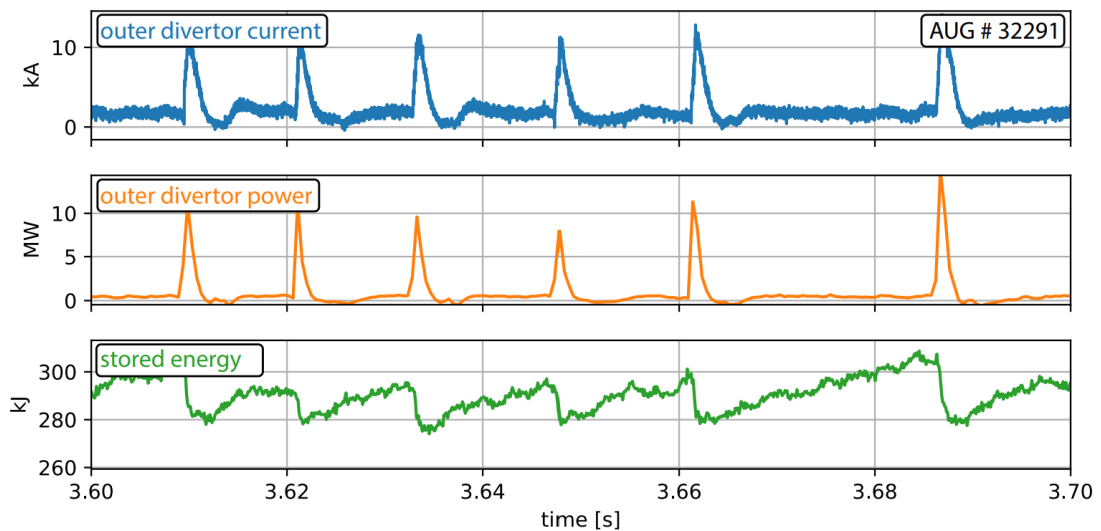


Figure 2.5: The divertor current (blue), total power on the outer divertor (orange) and total amount of stored energy in the plasma (green) shown in a small time window of discharge #32291 in ASDEX-Upgrade in a H-mode plasma [4].

The effect of the ELMs is shown in fig. 2.5. The ELMs cause a power load of over 5 MW on the divertor, causing the stored energy of the plasma to drop by 5-10%, which is slowly restored after the ELM [4].

ELMs can be divided in 3 main groups:

1. *Type-I* ELMs expel the highest amount of energy out of the confined plasma and need to be avoided in future fusion plants, because they reduce the lifetime of the divertor target plates [1]. They cause relative energy losses $\frac{\Delta W_{\text{ELM}}}{W_{\text{ped}}}$ of up to 20% [4]. They exhibit increasing frequency with increasing heating power [1].

2. *Type-II* ELMs expel less energy out of the plasma, they will be termed *quasi continuous exhausts* (QCE), since this is the common name for type-II ELMs in ASDEX-Upgrade [1].
3. *Type-III* ELMs exhibit a decreasing frequency with increasing heating power [1]. They occur after the L-H transition or at high density [1].

Since it is not possible in the data analysis of this thesis to distinguish between Type-I and Type-III ELMs, so they are collectively referred to as *ELMy*.

The *EDA H-mode* (enhanced D_α H-mode) is a special kind of H-mode plasma, without ELMs [1]. For EDA H-mode it appears that there is an edge instability, that enhances particle transport at the edge, without changing the energy transport, which allows them to avoid *ELMy* [1].

3 Scrape-off layer physics

The plasma edge region is of special interest, since the power exhaust takes place in this region. More precisely the power on one of the divertor targets is described by parallel component of the heat flux q . The heat flux ($q_{||}$), parallel to the magnetic flux surfaces, can be described by the following exponential function[5]:

$$q_{||} = q_{||0} e^{-r/\lambda_q}, \quad (3.1)$$

where r is the radial distance to the separatrix, λ_q the SOL power decay length and $q_{||0}$ the heat flux at the separatrix [2]. According to the following derivations, λ_q will be highly important for the power load on the divertor target plates. Since the parallel transport is orders of magnitudes faster than the perpendicular transport, the area on the divertor targets to which the power is distributed is very small, which concludes in a high power heat flux on the divertor [2]. Such a high power load can be problematic for future fusion devices. In the following sections the theoretical dependencies of λ_q will be derived, in order to know the behaviour of the heat flux in larger Tokamaks, because the area, on which the heat is distributed, is proportional to λ_q (see section 3.3).

3.1 Parallel heat flux

In the SOL the parallel heat flux is dominated by heat conduction, so convection will be neglected [1]. For conduction along the parallel coordinate $s_{||}$ of the SOL, the heat flux can be written with Fourier's law[2]:

$$q_{||} = -\kappa \frac{dT}{ds_{||}} = -\kappa_0 T^{5/2} \frac{dT}{ds_{||}} \quad (3.2)$$

This equation is valid for electrons and ions, T is the corresponding temperature and κ is the Spitzer-Härm thermal conductivity [1]. The constant κ_0 can be approximated by $2000 \frac{\text{W}}{\text{eV}^{7/2}\text{m}}$ for electrons and $60 \frac{\text{W}}{\text{eV}^{7/2}\text{m}}$ for the ions, which means that the total parallel heat flux is dominated by electron conduction [1].

3.2 Calculating $T(s_{||})$

In order to derive an expression for T out of eq. (3.2), one needs to consider two extreme scenarios, shown in fig. 3.1. In case (a) P_{SOL} (which is the power entering the SOL) enters entirely at the upstream end of the SOL, while in case (b) P_{SOL} enters uniformly along the length of the SOL. For both scenarios $q_{||}$ can be described by $q_{||} = \frac{P_{\text{SOL}}}{A_{||}}$, where $A_{||}$ is the total cross-sectional area perpendicular to the parallel heat flux in the SOL, which will be derived later [3].

For case (a) one starts with eq. (3.2) and integrates to find an expression for $T(s_{||})$. This leads to:

$$T(s_{||}) = \left(T_u^{7/2} - \frac{7 (P_{\text{SOL}}/A_{||}) s_{||}}{2 \kappa_0} \right)^{2/7} \quad (3.3)$$

Where T_u is the temperature at the upstream point in fig. 3.2. Integration along the opposite path gives:

$$T(s_{||}) = \left(T_t^{7/2} + \frac{7 (P_{\text{SOL}}/A_{||}) (L - s_{||})}{2 \kappa_0} \right)^{2/7} \quad (3.4)$$

Where T_t denotes the temperature at the downstream point, which is on the divertor target [3]. Since there are large temperature gradients along the SOL, like $T_u \gg T_t$, one can take eq. (3.4) and set $s_{||} = 0$, such that $T(0) = T_u$ and can neglect the $T_t^{7/2}$, because T_t is smaller than T_u [3]. This leads to the result for case (a):

$$T_u \approx \left(\frac{7 (P_{\text{SOL}}/A_{||}) L}{2 \kappa_0} \right)^{2/7} \quad (3.5)$$

For case (b), in which P_{SOL} enters uniformly along L , the heat-flux-gradient can be simplified [3]:

$$\frac{dq_{||}}{ds_{||}} = \frac{(P_{\text{SOL}}/A_{||})}{L} \quad (3.6)$$

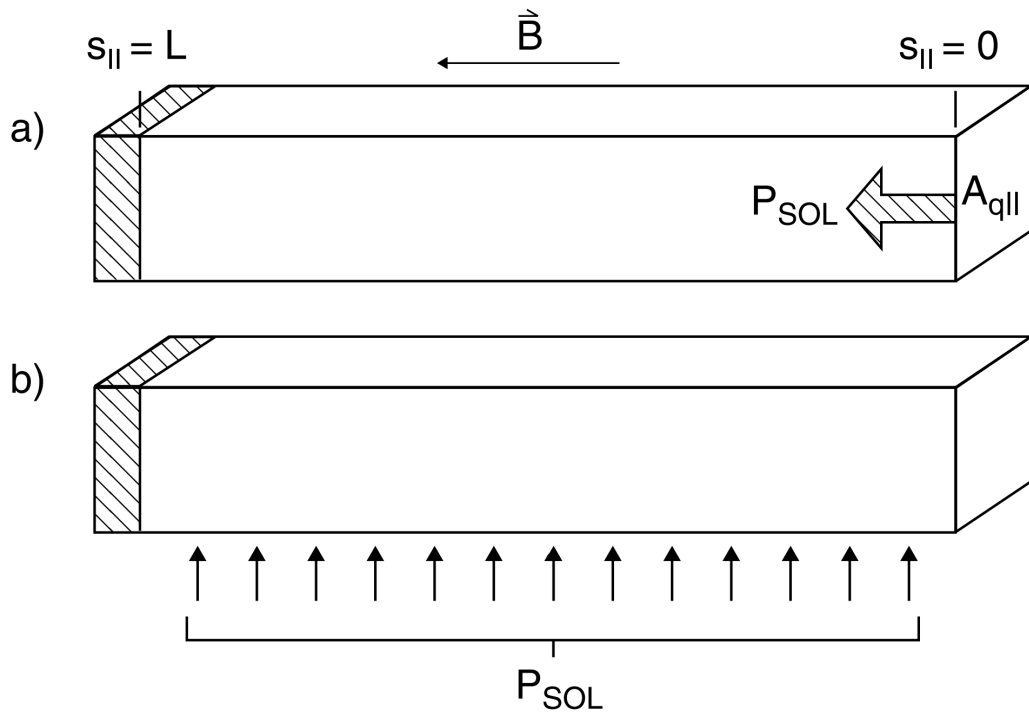


Figure 3.1: Two extreme scenarios for the power source of the SOL, P_{SOL} : (a) P_{SOL} enters at the upstream end and (b) P_{SOL} enters uniformly along the length of the SOL. The length L is the distance a particle travels in the SOL, until it reaches the divertor and s_{\parallel} is the coordinate along this path [3].

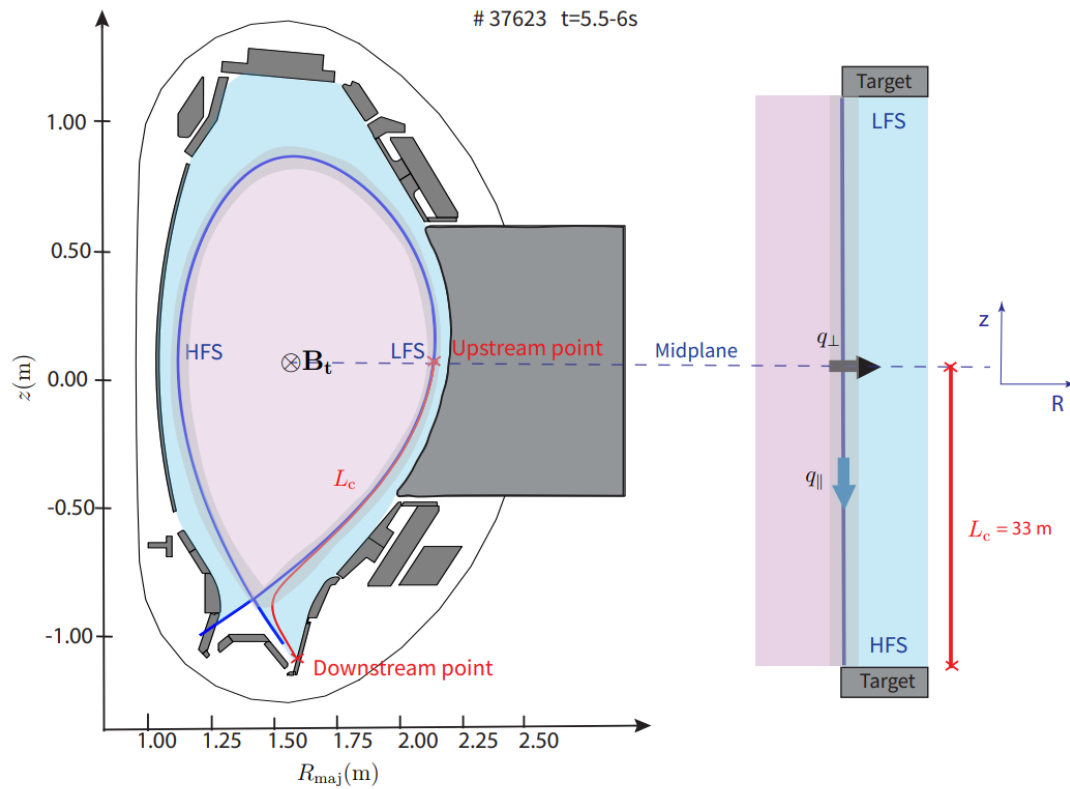


Figure 3.2: Geometry of the SOL in 2D (left), its simplified description (right), and the different heat fluxes with respect to the magnetic field lines. The separatrix is the blue region, the confined region is red and the SOL is light blue. This plot represents the plasma for the discharge #37623 at ASDEX Upgrade for $t=5.5-6$ s [2].

By integrating twice, one can solve eq. (3.2) for $T(s_{||})$:

$$T(s_{||}) = \left(T_u^{7/2} - \frac{7 (P_{\text{SOL}}/A_{||}) s_{||}^2}{4 L \kappa_0} \right)^{2/7} \quad (3.7)$$

and by integrating from the opposite direction [3]:

$$T(s_{||}) = \left(T_t^{7/2} + \frac{7 (P_{\text{SOL}}/A_{||}) (L - s_{||})^2}{4 L \kappa_0} \right)^{2/7} \quad (3.8)$$

Which leads, with analogous argumentation as before, to [3]:

$$T_u = \left(\frac{7 (P_{\text{SOL}}/A_{||}) L}{4 \kappa_0} \right)^{2/7} \quad (3.9)$$

The difference between this result and eq. (3.5) is only the factor $(1/2)^{2/7} \approx 0.82$, so the two very different models lead approximately to the same result.

By inserting eq. (3.1) in eq. (3.5) with $P_{\text{SOL}}/A_{||} = q_{||}$ one finds an expression for the temperature along the SOL [1]:

$$T = \left(\frac{7 q_{||0} L}{2 \kappa_0} \right)^{2/7} \exp\left(-\frac{2r}{7\lambda_{q||}}\right) := T_0 \exp\left(-\frac{r}{\lambda_{Te}}\right) \quad (3.10)$$

Where λ_{Te} is the electron temperature decay length at the outer midplane [1]. With this a relation between λ_{Te} and λ_q is obtained [1]:

$$\lambda_q = \frac{2}{7} \lambda_{Te} \quad (3.11)$$

This equation is also verified by the experimental data of ASDEX Upgrade tokamak [1].

Also eq. (3.11) is the motivation for this thesis: Since the heat flux on the divertor targets can potentially damage the material, it is important to know the dependencies of λ_q , in order to predict the heat flux on the divertor in ITER and future fusion devices. And eq. (3.11) shows that it is only necessary to know the dependencies of λ_{Te} , to predict λ_q . In this thesis, the dependencies of λ_{Te} will be analysed.

3.3 Theoretical dependencies of λ_{T_e}

The main idea in this derivation is to set the incoming power into the SOL equals the outgoing power, which means:

$$A_{\parallel}q_{\parallel} = A_{\perp}q_{\perp} \quad (3.12)$$

Here is q_{\parallel} the heat flux parallel to the magnetic field lines, q_{\perp} the heat flux perpendicular to the LCFS, A_{\perp} the area of the LCFS and A_{\parallel} the SOL cross-sectional area perpendicular to the magnetic field lines. This equation can easily be illustrated in fig. 3.2: All the power entering the SOL from the confined region, is flowing parallel to the magnetic field lines towards the divertor targets.

For this derivation all these four variables need to be expressed in geometrical and plasma's quantities.

First, A_{\perp} can be expressed easily. By approximating the tokamak's shape as a circular torus, one can just take a torus' surface with minor radius a and major radius R :

$$A_{\perp} = 2\pi R \cdot 2\pi a = 4\pi^2 Ra \quad (3.13)$$

Second, the parallel heat flux q_{\parallel} can be derived by using eq. (3.2), setting $T_t = 0$ and approximating a linear temperature profile from the upstream point to the divertor, which means: $\frac{dT}{ds_{\parallel}} = -\frac{T_u}{L}$. Now L can be simplified by $L = \pi R q_{95}$ [2], which results in the following:

$$q_{\parallel} = \kappa_0 T^{5/2} \frac{T_u}{\pi R q_{95}} \quad (3.14)$$

Third, the perpendicular heat flux can, like the parallel one, be described by Fourier's law: $q_{\perp} = -\kappa_{\perp} \frac{dT}{dr}$, where r is the radial coordinate. One can assume $T(r) = T_0 \exp\left(-\frac{r}{\lambda_{T_e}}\right)$ around the separatrix, which leads to the simplification: $\frac{dT}{dr} = -\frac{T_u}{\lambda_{T_e}}$ [2]. Also the perpendicular electron conduction in a plasma is related to a diffusion process of the electrons, which couples their diffusion and conduction constants:

$$\chi = \frac{\kappa}{n}, \quad (3.15)$$

where χ is the electrons thermal diffusivity and n their density [2]. This leads to the

final expression for the perpendicular heat flux:

$$q_{\perp} = n_u \chi \frac{T_u}{\lambda_{T_e}} \quad (3.16)$$

Fourth, the area of the SOL perpendicular to the magnetic field lines, A_{\parallel} needs to be expressed.

At first one needs to have a look at the plasma wetted area A_{wet} , which is the area of the divertor targets with plasma contact. This area is easily calculated by thinking of the radius of the plasma at the divertor targets as a ring, with circumference $2\pi R$ and width λ_q , since this defines the width of the SOL. The plasma wetted area of a target can therefore be approximated as $2\pi R\lambda_q$ and since there is an inner and outer divertor target, this leads to $A_{\text{wet}} = 4\pi R\lambda_q$, while approximating the same R for both targets [3].

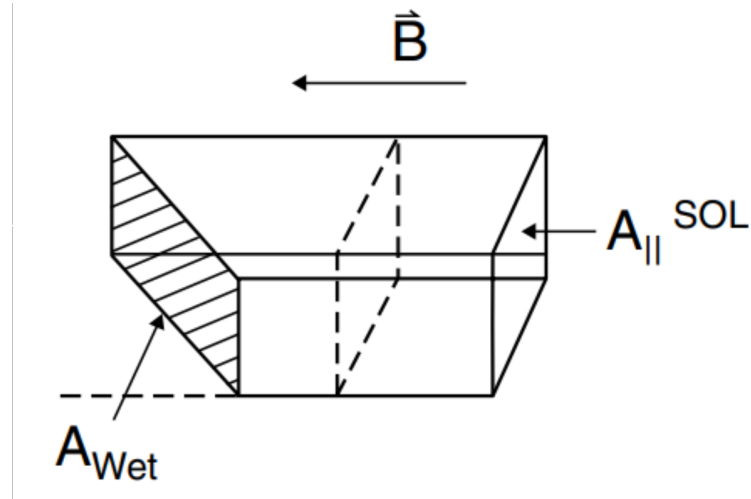


Figure 3.3: The plasma wetted area of the divertor targets A_{wet} and the area A_{\parallel} (here $A_{\parallel}^{\text{SOL}}$), perpendicular to the magnetic field \vec{B} [3].

Now one needs to have a look at the alignment of the divertor targets to the magnetic flux surfaces, which is illustrated in fig. 3.3. The area perpendicular to the magnetic field lines is calculated by

$$A_{\parallel} = \sin(\alpha) A_{\text{wet}}, \quad (3.17)$$

where α is not just the angle for the projection, but also the twisting angle of the

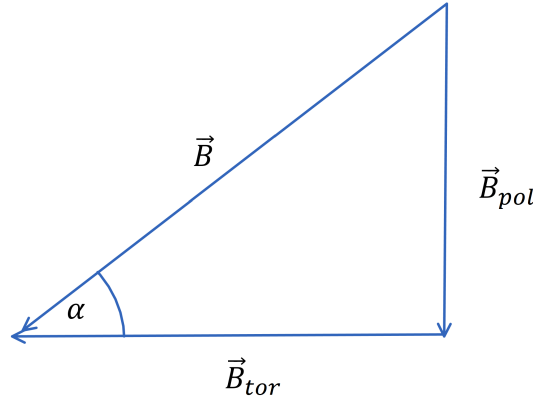


Figure 3.4: A magnetic field line with its components and the angle α .

magnetic field lines (see fig. 3.4). By thinking of the magnetic field as a vector with angle α to the toroidal plane, one can easily obtain the relation: $\sin(\alpha) = \frac{B_{pol}}{\|\vec{B}\|}$. Since $B_{tor} \gg B_{pol}$ one can approximate $\|\vec{B}\| = \sqrt{B_{tor}^2 + B_{pol}^2} \approx B_{tor}$. Inserting this into eq. (3.17) results in the final expression for $A_{||}$ [3]:

$$A_{||} = 4\pi R \lambda_q \frac{B_{pol}}{B_{tor}} \quad (3.18)$$

Now, after deriving expressions for $A_{||}$, A_{\perp} , $q_{||}$ and q_{\perp} they can be inserted into eq. (3.12), which says that the power in the SOL P_{SOL} is conserved and derive an expression for λ_{Te} . For this also eq. (3.11), $q_{95} \approx \frac{a}{R} \frac{B_{tor}}{B_{pol}}$ is used. Here T_{sep} is the temperature at the separatrix (expressed by eq. (3.5)). Since the upstream point is on the separatrix (see fig. 3.2), n_u will be replaced by the particle density at the separatrix n_{sep} and T_u and T by T_{sep} .

To sum up, one start with the power conservation:

$$A_{||} q_{||} = A_{\perp} q_{\perp} \quad (3.19)$$

and substituting equations (3.13), (3.14), (3.16) and (3.18) and $\lambda_q = \frac{2}{7} \lambda_{Te}$, which was 3.11, leads to:

$$\kappa_0 T_{sep}^{5/2} \frac{T_{sep}}{\pi q_{95} R} \frac{8}{7} \pi R \lambda_{Te} \frac{B_{pol}}{B_{tor}} = n_{sep} \chi \frac{T_{sep} 4\pi^2 a R}{\lambda_{Te}} \quad (3.20)$$

Now T_{sep} can be substituted using the result of the two-point-model in eq. (3.5) with

3 Scrape-off layer physics

$L = \pi R q_{95}$ [2], $q_{95} = \frac{a}{R} \frac{B_{\text{tor}}}{B_{\text{pol}}}$ and A_{\parallel} in eq. (3.18), which leads to:

$$T_{\text{sep}} = \left(\frac{49}{16} \frac{P_{\text{sep}}}{\lambda_{\text{Te}} \kappa_0} \frac{a}{R} \frac{B_{\text{tor}}^2}{B_{\text{pol}}^2} \right)^{2/7} \quad (3.21)$$

Inserting T_{sep} into eq. (3.20) and substituting χ with the assumption of Gyro-Bohm thermal diffusivity $\chi \propto \frac{T_{\text{sep}}}{B_{\text{tor}}}$ and again q_{95} with eq. (2.2) gives the fully substituted equation:

$$\kappa_0 \left(\frac{49}{16} \frac{P_{\text{sep}}}{\lambda_{\text{Te}} \kappa_0} \frac{a}{R} \frac{B_{\text{tor}}^2}{B_{\text{pol}}^2} \right)^{5/7} \frac{8}{7} \lambda_{\text{Te}} \frac{B_{\text{pol}}^2}{B_{\text{tor}}^2} \frac{R}{a} \propto \frac{n_{\text{sep}}}{B_{\text{tor}}} \left(\frac{49}{16} \frac{P_{\text{sep}}}{\lambda_{\text{Te}} \kappa_0} \frac{a}{R} \frac{B_{\text{tor}}^2}{B_{\text{pol}}^2} \right)^{2/7} \frac{4\pi^2 a R}{\lambda_{\text{Te}}} \quad (3.22)$$

Solving for λ_{Te} and dropping the constants leads to the final result for the dependencies of λ_{Te} :

$$\lambda_{\text{Te}} \propto n_{\text{sep}}^{\frac{7}{11}} \cdot \left(\frac{P_{\text{sep}}}{R} \right)^{-\frac{3}{11}} \cdot a \cdot B_{\text{tor}}^{\frac{1}{11}} \cdot B_{\text{pol}}^{-\frac{8}{11}} \quad (3.23)$$

Instead of B_{pol} the plasma current $I_p \propto B_{\text{pol}}$ will be used, which results in:

$$\lambda_{\text{Te}} \propto n_{\text{sep}}^{\frac{7}{11}} \cdot \left(\frac{P_{\text{sep}}}{R} \right)^{-\frac{3}{11}} \cdot a \cdot B_{\text{tor}}^{\frac{1}{11}} \cdot I_p^{-\frac{8}{11}} \quad (3.24)$$

This result will be compared to the measured results in the following chapters. A similar calculation is done in [6].

Also the exponential decay lengths λ_n with $n(r) = n_0 \exp\left(-\frac{r}{\lambda_n}\right)$ and λ_p with $p(r) = p_0 \exp\left(-\frac{r}{\lambda_p}\right)$, where $p(r)$ is the electron pressure and λ_p the electron pressure decay length, will be investigated for the measured discharges.

4 Methodology

4.1 The Thomson Scattering system in ASDEX-Upgrade

Through the Thomson Scattering (TS), which is based on the elastic scattering of a photon with an electron, where the photon is re-emitted with the same wavelength, but in an arbitrary direction, one can measure the electron's temperature and particle density [2]. Since the temperature of the electrons is linked to their velocity, one can analyse the Doppler broadening of the re-emitted photon to calculate the temperature, by assuming a Maxwellian distribution function [1] and the particle density can be reconstructed by the intensity of scattered light [2].

At AUG there are six monochromatic Nd:YAG lasers (vertically launched) penetrating the electrons in the plasma edge region, consisting partly of the confined plasma and partly of the SOL (see fig. 4.1). Each of them has a wavelength of 1064 nm, a pulse energy beneath 1 J and a pulse rate of 20 Hz, where each pulse has a duration of 1 ns [2]. These six lasers run equally spaced in time, therefore a pulse rate of 120 Hz at the edge is obtained [1]. The scattering volumes in fig. 4.1 allow a spacial resolution of 3 mm [2] and since the steep temperature and density gradients at the plasma edge are about 2 cm wide, they can be spatially resolved by the TS system [1].

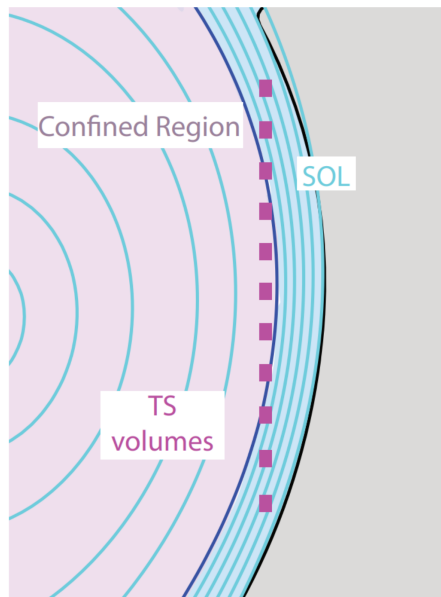


Figure 4.1: A poloidal cross section of the Thomson Scattering system at the plasma edge region of the ASDEX-Upgrade Tokamak. The dashed purple line shows the measurement volumes, located vertically in the poloidal plane. The confined region is here colored in red and the SOL in blue [2].

4.2 Calculation of the decay lengths λ_{Te} and λ_n

In order to calculate λ_{Te} and λ_n from the raw Thomson Scattering data, the first step is mapping. Since the Thomson Scattering gives only values in cylindrical coordinates, with a ρ and z coordinate, these coordinates are mapped to calculate a normalized distance to the plasma core in the poloidal plane. And this new radial coordinate is again mapped, but this time along the toroidal plane, in order to receive a non-normalized major radius. This is the new Radius, now the data can be ordered along the distance to the plasma core or the tokamak's center.

In the next step the data is filtered. All data points with unreasonable high or low temperature or density are neglected, since they have to be error measurements. In particular these are all temperatures above 500 eV and below 10 eV and all particle densities below $1 \cdot 10^{18} \text{ 1/m}^3$. Also the times when ELMs occur and lastly the data with unreasonable errors are excluded. With T as the the electron temperature and ΔT as its the standard deviation, one can define the relative error as $\frac{\Delta T}{T}$ and each value with a relative error higher than 0.9 is excluded. This ends the first filtering process.

Then the exponential fit is prepared. At first the temperature at the separatrix T_{sep} is calculated by using eq. (3.5), but in a more accurate version than eq. (3.21) with some more geometrical corrections. For this L is substituted with $\pi q_{cyl} R$, where

$$q_{cyl} = \frac{B_{tor}}{\langle B_{pol} \rangle} \hat{\kappa} \quad (4.1)$$

,with $A = \frac{R}{a}$, is the cylindrical safety factor, which takes also into account the elongation of the plasma shape [7]. Here $\hat{\kappa}$ is defined as $\hat{\kappa} = \sqrt{\frac{1+\kappa^2}{2}}$, with the elongation of the plasma κ , and $\langle B_{pol} \rangle$ is the mean poloidal magnetic field, defined as [7]:

$$\langle B_{pol} \rangle = \frac{\mu_0 I_p}{2\pi a \hat{\kappa}} \quad (4.2)$$

And for $A_{||}$ the expression $A_{||} = 4\pi R \langle \lambda_q \rangle \frac{\langle B_{pol} \rangle}{B_{tor}}$ is inserted, where $\langle \lambda_q \rangle$ is the poloidally averaged λ_q [7]. This leads to the expression that is used to estimate T_{sep} [1]:

$$T_{sep} = \left(\frac{7 P_{sep} q_{cyl}^2 A}{2 \kappa_0 \hat{\kappa} \langle \lambda_q \rangle} \right)^{2/7} \quad (4.3)$$

Then the radius of the separatrix r_{sep} is estimated by taking the median of all radii of the Thomson Scattering data, but only if the corresponding temperature is in the range of 33 eV around T_{sep} . Taking the median has advantages over the mean value, since it is more robust against scattering. This leads to the first approximation of the separatrix position.

However, this first approximation is just a tool for a better one, using a similar filtering. This time one takes the median of all values with lower temperature difference than 13 eV with respect to T_{sep} and with lower radial distance than 9 mm to the first approximation of r_{sep} . This leads to a robust approximation for the real separatrix position.

With this estimated separatrix position a second filtering process of the data is executed. Only the data within a radius between 5 mm inside of the second estimated separatrix position and 11 mm outside is taken. Also the values with a temperature higher than 280 eV are neglected, since such a high temperature at the plasma edge is unreasonable. A similar filtering is done for the particle density with a radial range of 5 mm inside and 12 mm outside and a density limit of $6.5 \cdot 10^{19} \text{ 1/m}^3$.

With this filtered data, the first fit is executed. This fit has the form $T_{\text{TS}}(r) = T_{\text{sep}} \cdot \exp(-(r_{\text{TS}} - x_1)/x_2)$, where r_{TS} is the radius and T_{TS} is the temperature of the Thomson Scattering data points. This results in the two fitting parameters $x_1 = r_{\text{sep}}$ and $x_2 = \lambda_{\text{Te}}$. This first fit was just to find the separatrix position, so that one need no longer to work with the approximations. This result of the fit will be treated as the real separatrix position. The λ_{Te} is not used for anything.

In order to do the second fit for λ_{Te} a third filtering process starts. The raw data for this filtering is the data after the first filtering and before the second. Here basically the second filtering is repeated with the new separatrix position. In this filtering all values with radius smaller than 5 mm than the separatrix or larger than 9 mm or with temperature higher than 280 eV are neglected for the temperature fit. For the density fit it is almost the same, the allowed inner radius is also 5 mm and the outer radius is 12 mm and the maximum limit for n is as before $6.5 \cdot 10^{19} \text{ 1/m}^3$. In both filtering processes it is secured that the data is reasonable. This is done by neglecting all values with a temperature lower than 20 eV and position inside the confined region or temperature higher than 80 eV and position more than 5 mm outside the separatrix or temperature higher than 60 eV and position more than 10 mm outside

the separatrix. This filterings are illustrated in fig. 4.2 for the temperature and in fig. 4.3 for the density.

With the remaining data points the second fit is executed. It has the same form as before: $T_{TS}(r) = T_{sep} \cdot \exp(-(r_{TS} - x_1)/x_2)$ with $x_1 = r_{sep}$ and $x_2 = \lambda_{Te}$, but this time λ_{Te} is the final decay length for the temperature, which will be used in all further calculations. The next and last step is the third fit for λ_n of the form: $T_{TS}(r) = x_1 \cdot \exp(-(r_{TS} - r_{sep})/x_2)$ with $x_1 = n_{sep}$ and $x_2 = \lambda_n$. This non-linear fits are also shown in fig. 4.2 and fig. 4.3.

This leads to the final result of the decay lengths. In the next section the properties I_p , P_{sep} , n_{sep} and B_{tor} of each measured discharge (shot) are taken to determine the dependencies of the decay lengths.

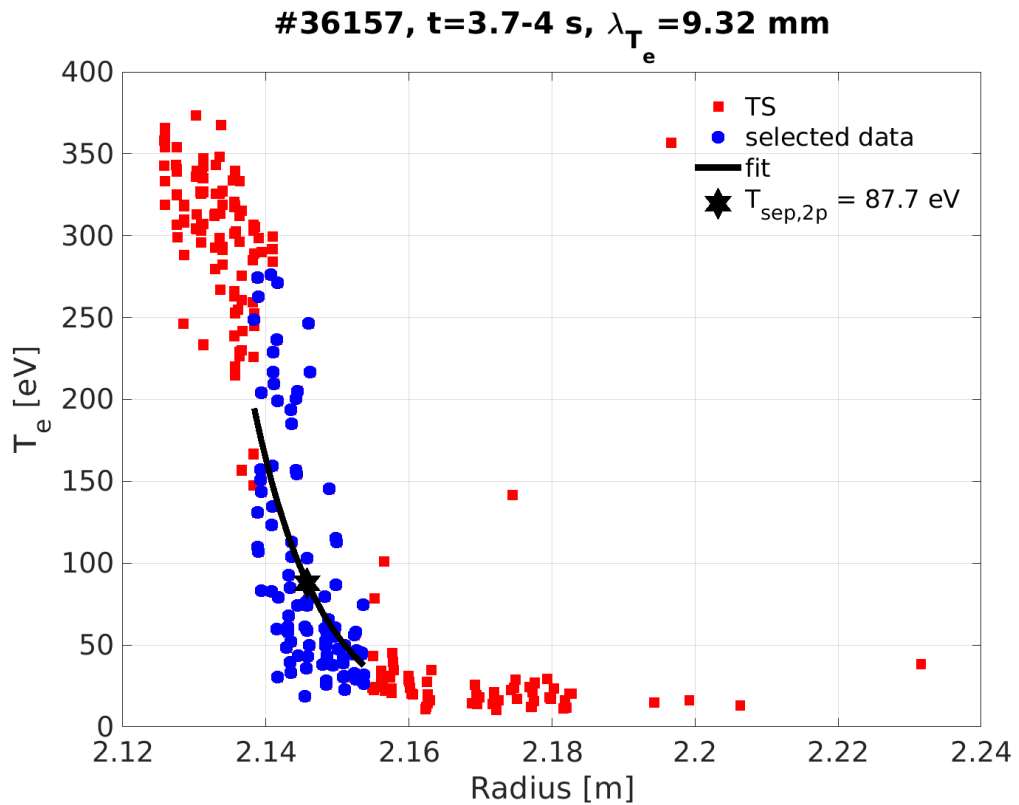


Figure 4.2: Thomson scattering data and non-linear fit for shot #36157 in the time window $t = 3.7 - 4$ s. T_{sep} is marked with a black star, its value is calculated by eq. (3.5) which is the result of the two point model and its position is determined through a non-linear fit. The fit for λ_{T_e} is shown as a black line. Here one can see all the filters applied. Only the blue data points count into the fit, the other TS-data is neglected, because it is over $T = 280$ eV, or more than 5 mm to the left or 9 mm to the right of the separatrix position. Also the unreasonable values, which would contradict the decay at the edge are neglected, but in this picture there are none of them.

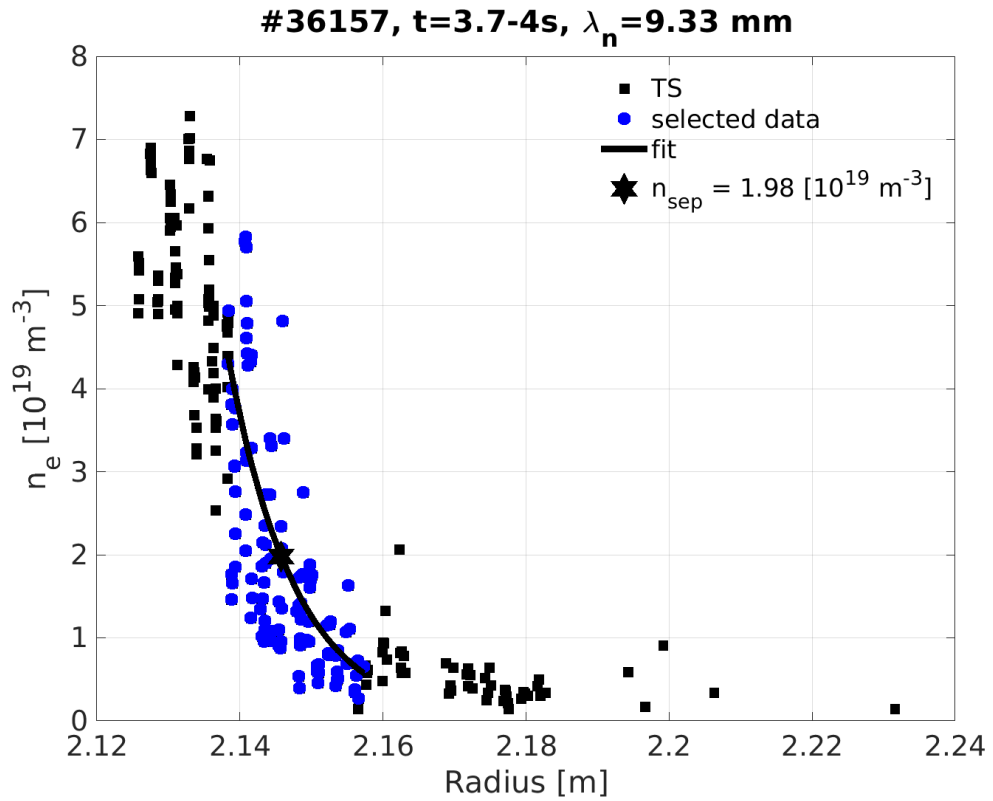


Figure 4.3: TS-data and non-linear fit for the density in the example of shot #36157 $t = 3.7 - 4$ s. The separatrix (black star) density is calculated by the fit, which is shown as a black line. All the data higher than $6.5 \cdot 10^{19} \text{ 1/m}^3$ or further on the left of the separatrix than 5 mm or on the right than 12 mm or not reasonably decaying at the edge, are neglected and therefore marked in black, while not neglected data is marked in blue.

4.3 Impact of the radial interval on the decay lengths

After the filtering processes one could ask if the allowed distance of the TS data to the separatrix is well chosen. The inner radius R_{in} and outer radius R_{out} determine how far inside or outside the separatrix a TS data point can be to be still included in the fitting process. Obviously increasing these radii includes more data points, but one also moves the region under analysis further away from the separatrix and the near-SOL.

In order to check the sensitivity of the decay lengths to the radii, the distribution of the decay lengths for different R_{in} and R_{out} are shown in fig. 4.4 and fig. 4.5. In these plots different values for R_{in} and R_{out} for λ_{Te} (blue) and for λ_n (red) are compared.

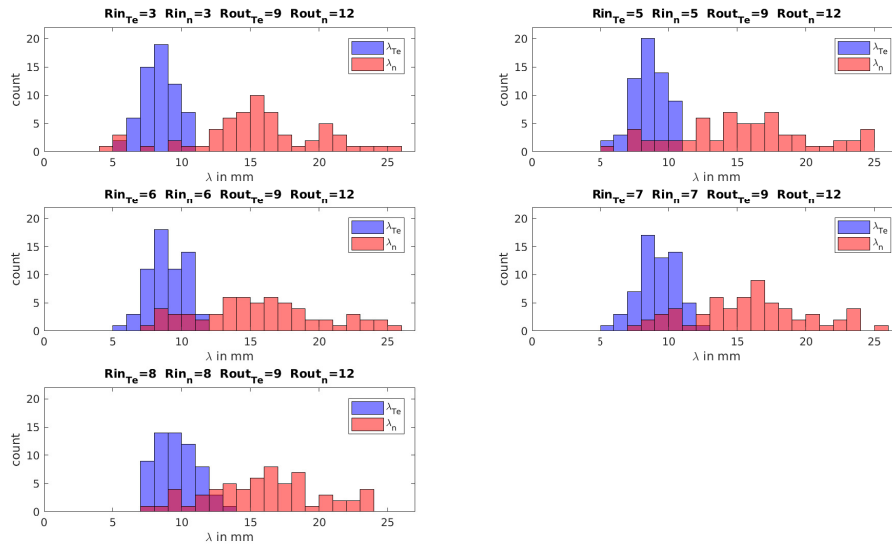


Figure 4.4: Histograms for determined decay lengths of all discharges with varied inner radii $R_{in_{Te}}$ and R_{in_n} . This means that each value further inside of r_{sep} than $R_{in_{Te}}$ for λ_{Te} and R_{in_n} for $R_{in_{Te}}$ is neglected. All values for R_{in} and R_{out} are in mm.

Looking at the pictures in fig. 4.4 with constant R_{out} and varied R_{in} one can see that the distribution of λ_{Te} peaks around $\lambda_{Te} = 8$ mm for $R_{in_{Te}} = 3$ mm and 5 mm, while for larger values of $R_{in_{Te}}$ the distribution gets broader. For λ_n the distribution doesn't change much. It is noticeable that the narrowest distribution is obtained with

4 Methodology

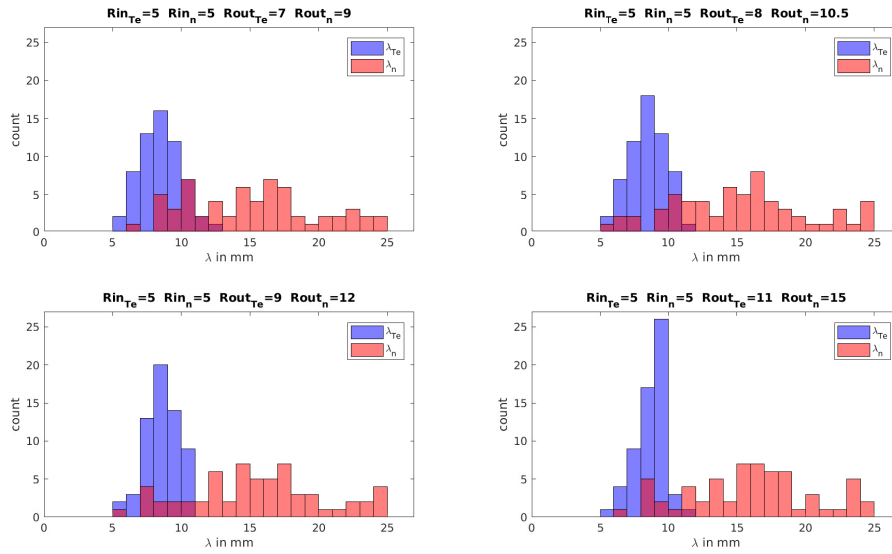


Figure 4.5: Histogram for the decay lengths of all discharges with variations of the outer radii $Rout_{Te}$ and $Rout_n$, where all values are in mm.

$\lambda_n = 3$ mm.

The histograms for the variation of $Rout$ in fig. 4.5 show that there is also not much change in the variation of $Rout_{Te}$, except for $Rout_{Te} = 11$ mm, there the peak gets higher and the right side of this peak almost vanishes. For λ_n the distribution is again wide and there is no significant change with changing $Rout_n$.

5 Results

5.1 Database description

In this section the database in this thesis will be introduced and the variation of the parameters of the analysed discharges will be shown. Discharges are classified as: ELMy, QCE and EDA H-mode.

The whole database consists of 61 discharges, each with a measured time window of around 0.2 s to 0.3 s. The following pictures give an idea of the variation of the plasma parameters in this database.

Fig. 5.1 depicts I_p vs. B_{tor} and shows that there is not a continuous variation of I_p , but 5 different values for it. There is no correlation between I_p and B_{tor} , they are independent plasma parameters.

The next plot is fig. 5.2, where q_{95} is plotted against B_{tor} . Here it is important to keep eq. (2.2) on page 5 in mind, which shows that q_{95} is rising with and B_{tor} and falling with I_p , since $I_p \propto B_{pol}$. Even though I_p is not constant, fig. 5.2 shows an increasing q_{95} with increasing B_{tor} . For the understanding of the figure it is necessary to know that all values of q_{95} in this thesis are actually negative and only the absolute value is plotted.

Fig. 5.3 shows P_{sep} vs. n_{sep} . As mentioned in section 4.2 the value of n_{sep} is a byproduct of the exponential fit for the particle density along the SOL. The only quantity with a mentionable error so far is P_{sep} , which is calculated by subtracting the total input power into the plasma of the radiated power out of the plasma.

The last of the four plots shows n_{sep} vs. T_{sep} , which is in fig. 5.4. These two quantities are linked to the exponential fits, as shown in section 4.2.

5 Results

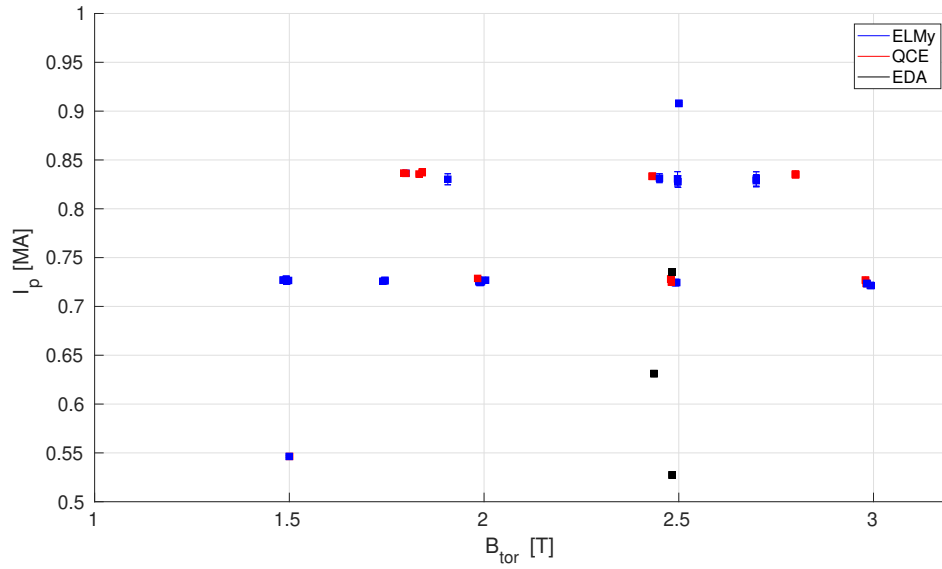


Figure 5.1: The plasma current I_p plotted against the toroidal magnetic field B_{tor} .

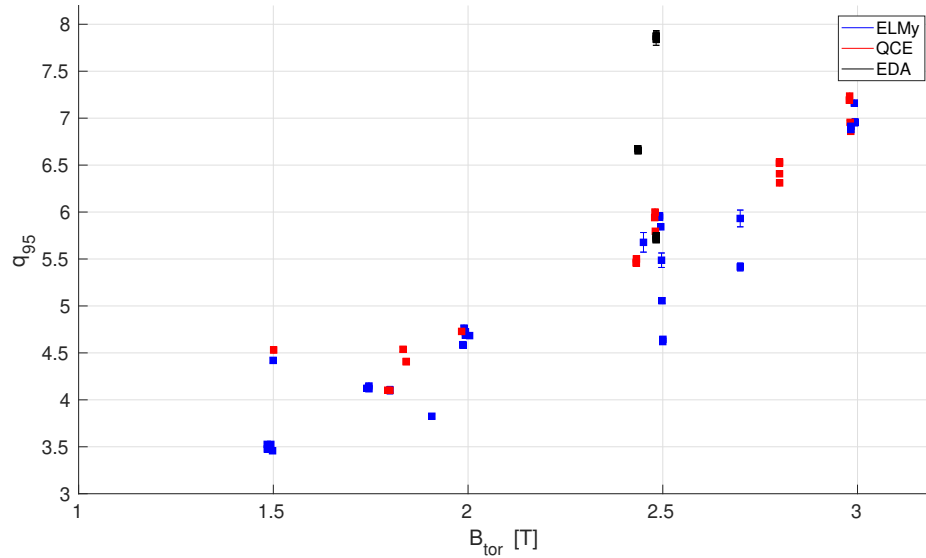


Figure 5.2: The safety factor q_{95} at $\rho_{\text{pol}} = 0.95$ plotted against the toroidal magnetic field B_{tor} .

5 Results

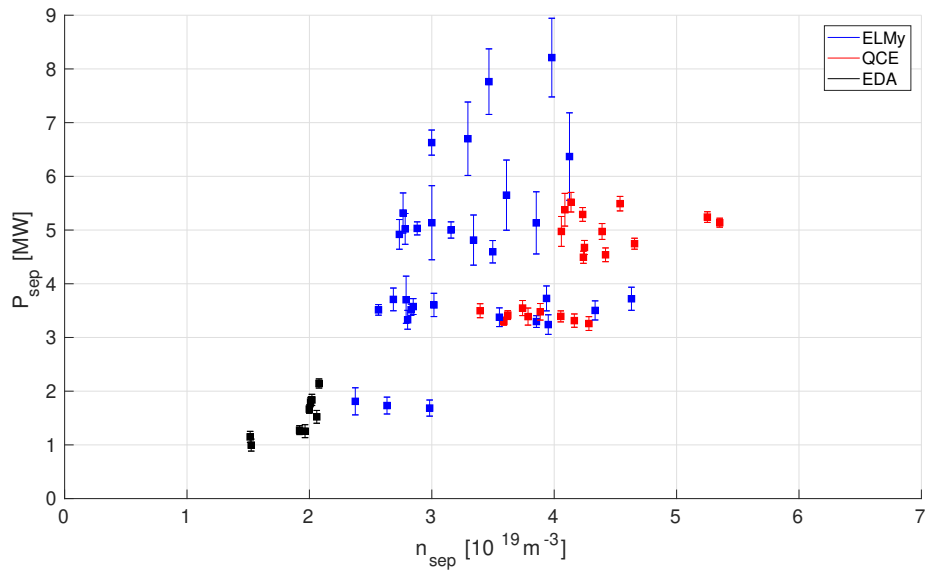


Figure 5.3: The power crossing the separatrix P_{sep} plotted against the electron density n_{sep} at the separatrix.

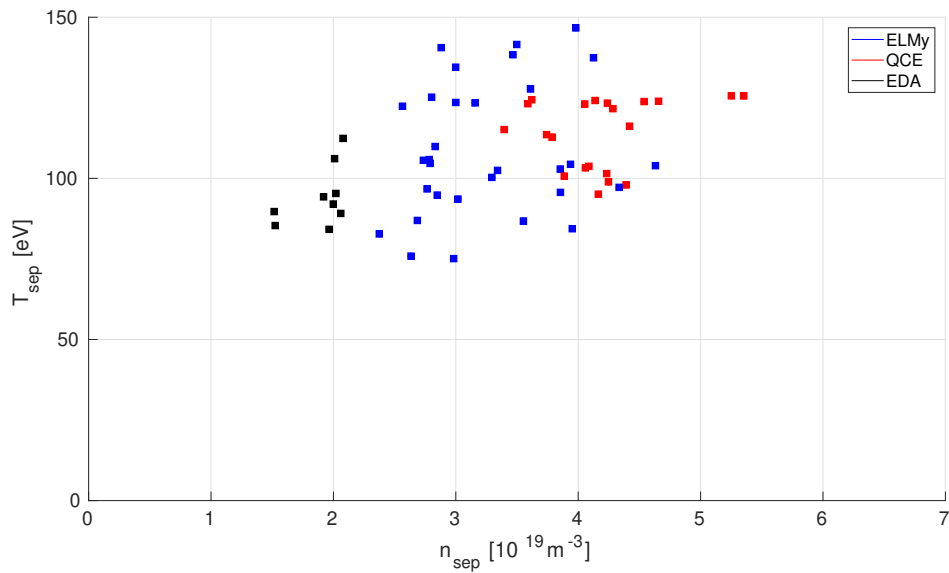


Figure 5.4: The separatrix temperature T_{sep} against the electron particle density n_{sep} at the separatrix. The separatrix temperature is calculated through the formula in eq. (3.5) and the density is a result of the exponential fit.

5.2 Scrape-off layer decay lengths

In this section the dependencies of the decay lengths will be determined. First, one defines a new decay length: $\lambda_p := \frac{1}{\frac{1}{\lambda_{Te}} + \frac{1}{\lambda_n}}$. This is the decay length of the electron pressure p , which is assumed to decay in the SOL in the same way as n and T . This matters because there could be some kind of λ_p dependency in λ_q and not just a λ_{Te} dependency as derived in eq. (3.11). Such a possible dependency is described in [6].

The plots of all decay lengths versus the separatrix density is shown in fig. 5.5. The uncertainties in this plots for λ_{Te} and λ_n are calculated thought the errors of the fit parameters and for λ_p thought the error propagation. This plot shows that λ_n is

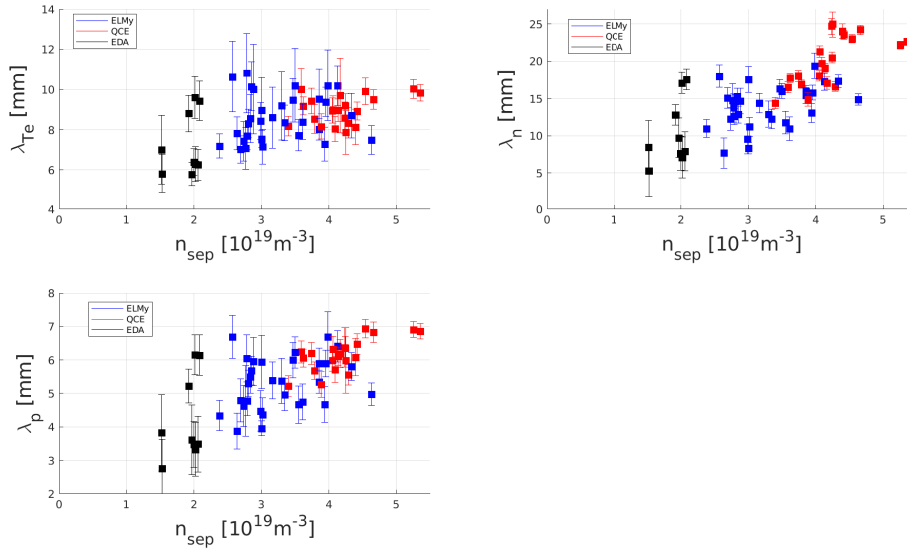


Figure 5.5: The different decay lengths plotted against n_{sep} .

increasing with increasing n_{sep} . For λ_{Te} the dependency is much weaker. λ_p shows instead a clear dependency with n_{sep} .

Now one can define the ion poloidal gyro-radius $\rho_{s,pol}$ according to [8] as:

$$\rho_{s,pol} = \frac{\sqrt{m_D \cdot T_{sep}}}{e \cdot \langle B_{pol} \rangle} \quad (5.1)$$

where e is the electron charge and m_D the mass of deuterium. All values are in-

serted in SI units. This radius can be used to normalize the decay lengths, which are depicted in fig. 5.6, where the normalized decay lengths are plotted vs. n_{sep} . While the dependency between λ_n and n_{sep} does not substantially change when λ_n is normalized to $\rho_{\text{s,pol}}$, the correlation between λ_{Te} and n_{sep} improves when λ_{Te} is normalized to $\rho_{\text{s,pol}}$. As a consequence, a stronger correlation between λ_p and n_{sep} is found when λ_p is normalized to $\rho_{\text{s,pol}}$.

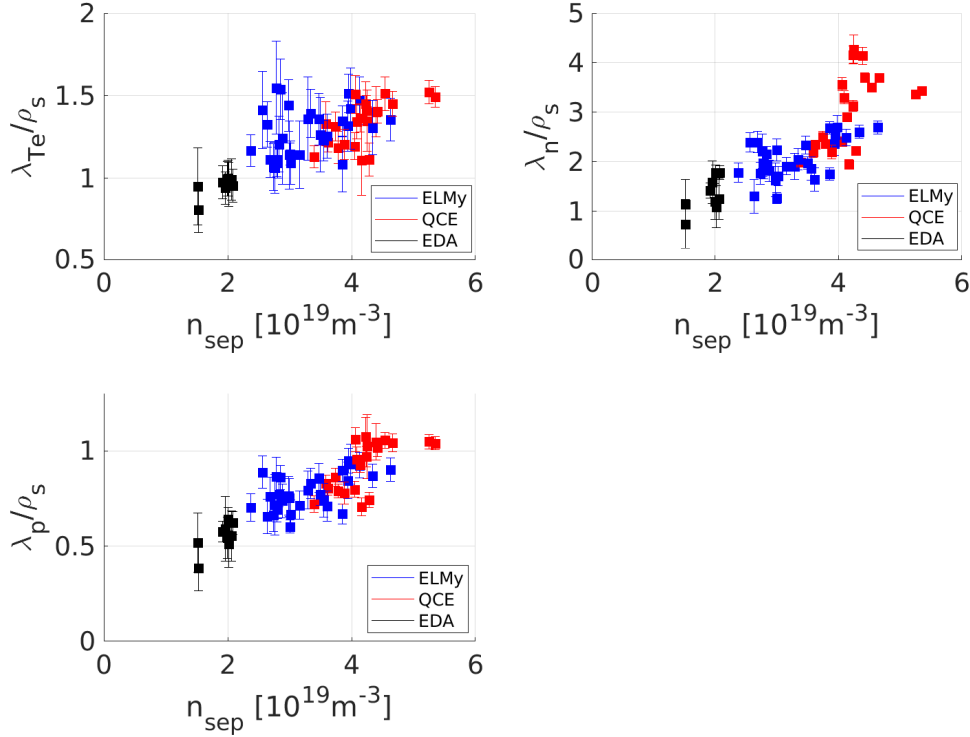


Figure 5.6: The decay lengths normalized to $\rho_{\text{s,pol}}$ against n_{sep} .

Another important parameter that characterizes the plasma edge turbulent regime is α_{T} , which is here calculated as:

$$\alpha_{\text{T}} = 3.1 \cdot 10^{-18} R q_{\text{cyl}}^2 \frac{n_{\text{sep}}}{T_{\text{sep}}^2} Z_{\text{eff}} \quad (5.2)$$

where Z_{eff} is the effective particle charge [8]. All quantities need to be inserted in SI units, except for T_{sep} , which is in eV. The three decay lengths vs. α_{T} are depicted in fig. 5.7. There is no clear dependency of any decay length on α_{T} . When normalized by $\rho_{\text{s,pol}}$ there is, still no dependency of α_{T} , as it can be seen in fig. 5.8.

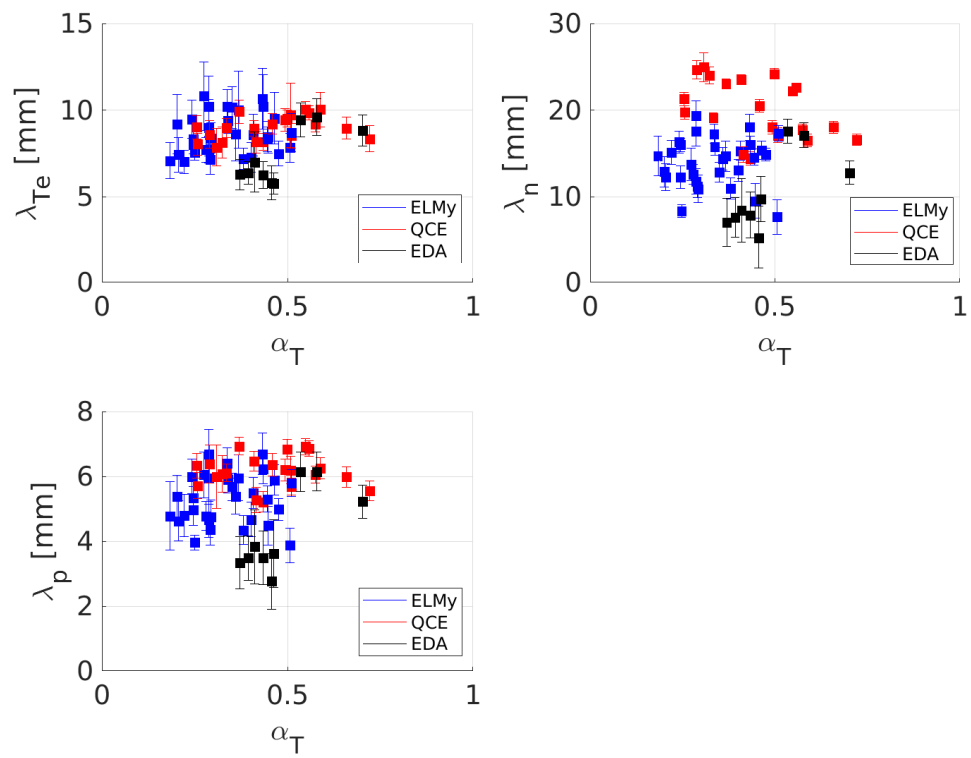


Figure 5.7: The different decay lengths plotted against α_T .

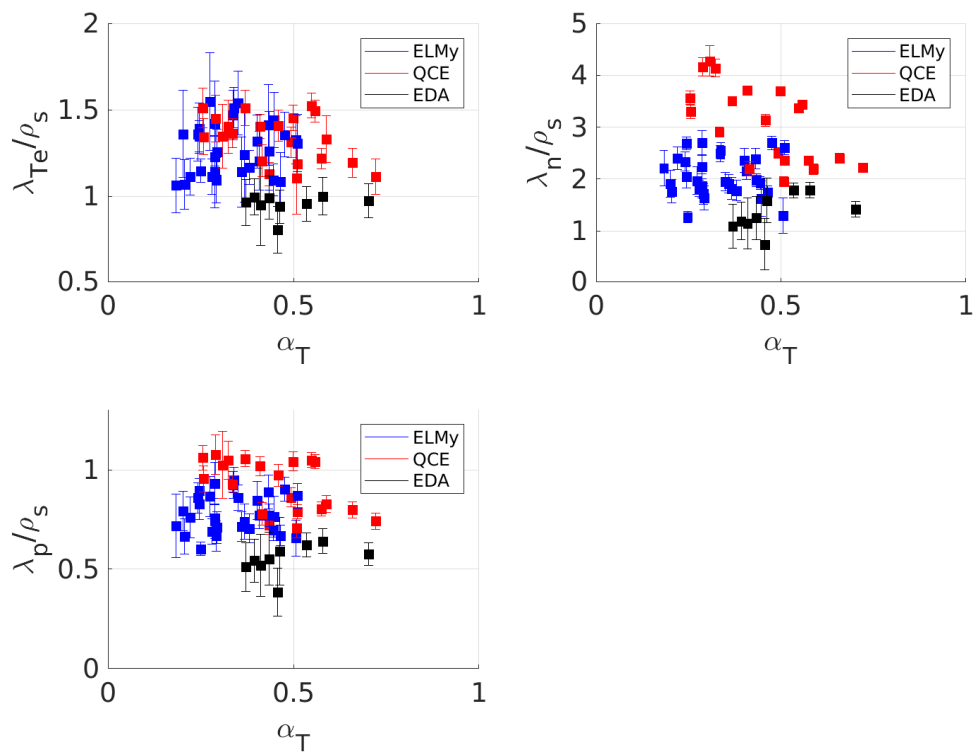


Figure 5.8: The different decay lengths normalized by $\rho_{s,pol}$ plotted against α_T .

Fig. 5.9 shows λ_n and λ_{Te} plotted against each other. Also in fig. 5.9 three lines representing different gradient length ratios $\eta = \frac{\lambda_n}{\lambda_{Te}} = 1$ (solid), $\eta = 2$ (dashed), $\eta = 3$ (dashed-dotted) are depicted. A similar plot can be found in [7] and [6].

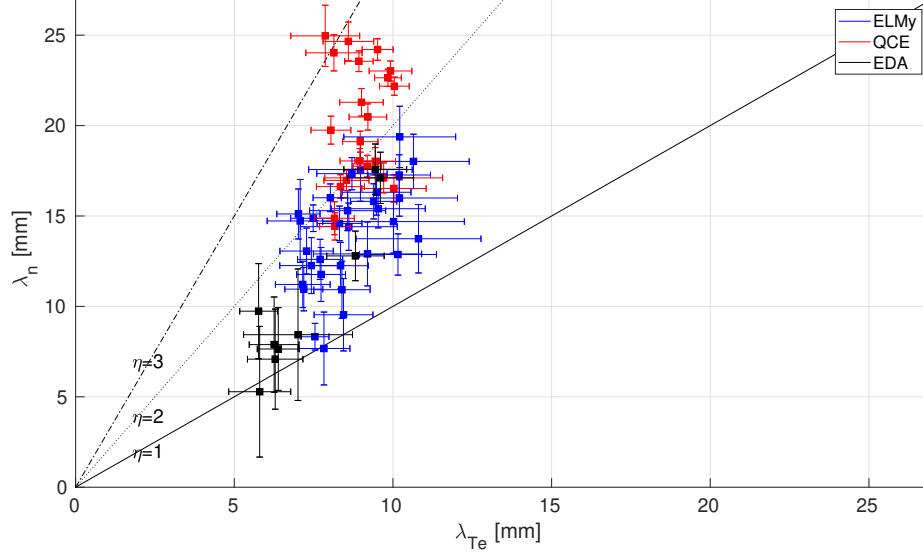


Figure 5.9: λ_{Te} vs. λ_n . Here three lines with constant $\eta := \frac{\lambda_n}{\lambda_{Te}}$ are shown in order to rate the ratio between the decay lengths.

There is no recognizable dependency between the decay lengths, but clearly the ELMMy H-mode and EDA H-mode discharges have a η between 1 and 2, while for the QCE discharges the η is beyond 2. This means that QCE ELMs lead to a higher λ_n , while not really changing the λ_{Te} .

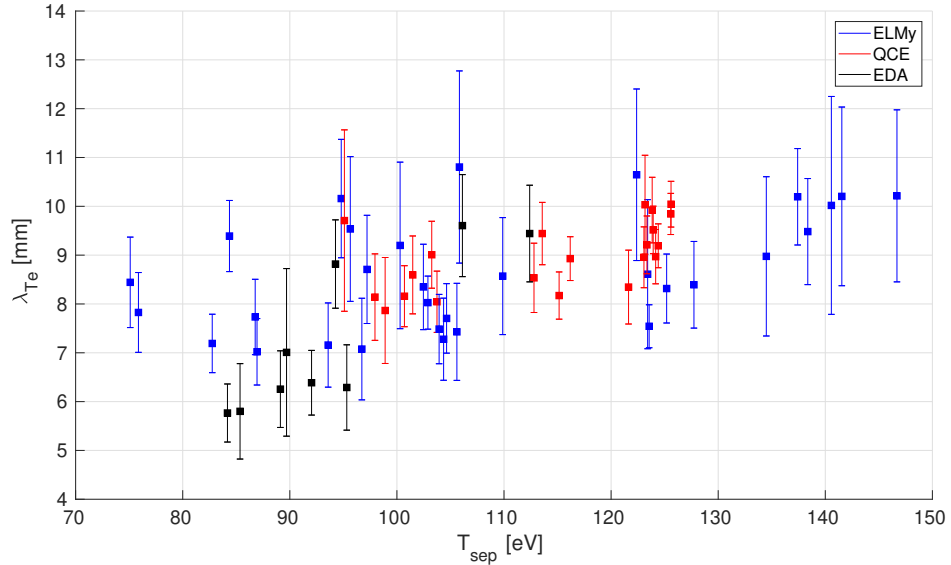
λ_{Te} vs. T_{sep} is shown in fig. 5.10. No clear correlation can be seen between λ_{Te} and T_{sep} in the analysed dataset.

The core of this thesis, the most important plot is shown in fig. 5.11. This figure shows the dependencies of λ_{Te} . From eq. (3.24) follows the fit equation:

$$\lambda_{Te} = x_1 \cdot n_{sep}^{x_2} \cdot P_{sep}^{x_3} \cdot B_{tor}^{x_4} \cdot I_p^{x_5} \quad (5.3)$$

Where x_i ($i \in \{1, \dots, 5\}$) are the fit parameters, which determine the experimental dependencies. The result of the non-linear-fit is (as mentioned in fig. 5.11):

$$\lambda_{Te} = (3.39 \pm 0.37) \cdot B_{tor}^{0.24 \pm 0.06} \cdot I_p^{-0.79 \pm 0.12} \cdot P_{sep}^{0.2 \pm 0.04} \cdot n_{sep}^{0.2 \pm 0.06} \quad (5.4)$$


 Figure 5.10: Plot of λ_{Te} vs. T_{sep}

where the accuracy of the non-linear-fit is determined through $R^2 = 0.63$. For this equation n_{sep} needs to be inserted in 10^{-19}1/m^3 , P_{sep} in MW, B_{tor} in T and I_p in MA. The resulting λ_{Te} will be given in mm. To be able to distinguish in a unique way, the λ_{Te} , which is determined of the exponential fit of the TS data, will be called "measured" λ_{Te} , while the λ_{Te} that results out of eq. (5.4) when the plasma parameters of a discharge are inserted, will be termed "fitted" λ_{Te} .

Now, when comparing the result of the non-linear fit in eq. (5.4) with the theoretical dependencies in eq. (3.24), then one find for the theoretical the dependency of I_p the value $-8/11 \approx -0.72$, which is included in the errorbounds of -0.79 ± 0.12 . The expected value for B_{tor} would be $1/11 \approx 0.09$, while the here found value is 0.24 ± 0.06 . The theoretical value is not included in the error bounds, but it is still the right sign and dimension. For P_{sep} the exponent $-3/11 \approx -0.27$ is delivered by the theory, but a value of 0.2 ± 0.04 is found. Here the theoretical value is far from being in the error bars of the fitted value, and the sign is reversed. Ultimately n_{sep} has the theoretical value $7/11 \approx 0.64$, while the measured value is 0.2 ± 0.06 , which is clearly not in the errorbounds and doesn't match the theoretical value by the factor 3.2.

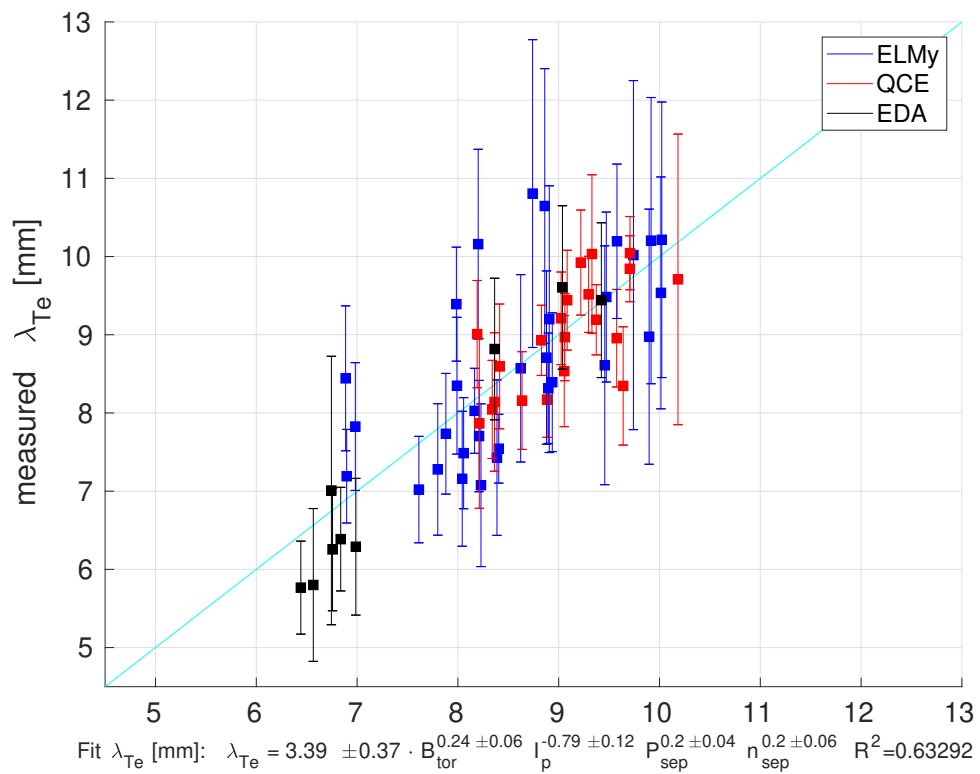


Figure 5.11: Here the resulting fit-equation of the non-linear fitted λ_{Te} is evaluated at the plasma parameters for each data point and plotted against the measured value for λ_{Te} . The cyan line has slope 1, which means each point located on it has the same measured λ_{Te} as the non-linear-fit leads to.

5.3 λ_{Te} trends at constant I_p

In this last two sections the dependencies of λ_{Te} for discharges with constant plasma parameters are shown. Another plasma parameter to introduce here is the amount of deuterium inserted into the tokamak, this is called D_{tot} or "gas-puff" and is measured in the unit of electrons/s. To keep specific plasma parameters constant and look at the dependencies of λ_{Te} of the other non-constant parameters, also D_{tot} will be held constant.

The first group of discharges has $I_p = 0.83$ MA and $D_{tot} = 3 \cdot 10^{22}$ electrons/s and is shown in fig. 5.12 and fig. 5.13. Compared to fig. 5.3, where P_{sep} is in the interval of 1 MA to 8 MA and n_{sep} in the interval of $1.5 \cdot 10^{19} m^{-3}$ to $5.5 \cdot 10^{19} m^{-3}$, for this group P_{sep} and n_{sep} are more or less constant. Since also I_p and D_{tot} are held constant, the only changing variable is B_{tor} , therefore in fig. 5.13 the B_{tor} dependency of λ_{Te} is shown. By looking at this picture, a trend of rising λ_{Te} with increasing B_{tor} is observed. This group can be seen as representative example of all discharges with QCE ELMs.

Another group of discharges with constant $I_p = 0.725$ MA and $D_{tot} = 3 \cdot 10^{22}$ electrons/s and P_{sep} in the range between 3 MW and 4 MW, which means P_{sep} more or less constant, is shown in fig. 5.14 and fig. 5.15. From fig. 5.14 one observes additionally that n_{sep} is relatively constant (compared to 5.4). As a result, fig. 5.15 shows again a trend for increasing λ_{Te} with increasing B_{tor} , but this time not only for QCE discharges, but also for ELMy H-modes.

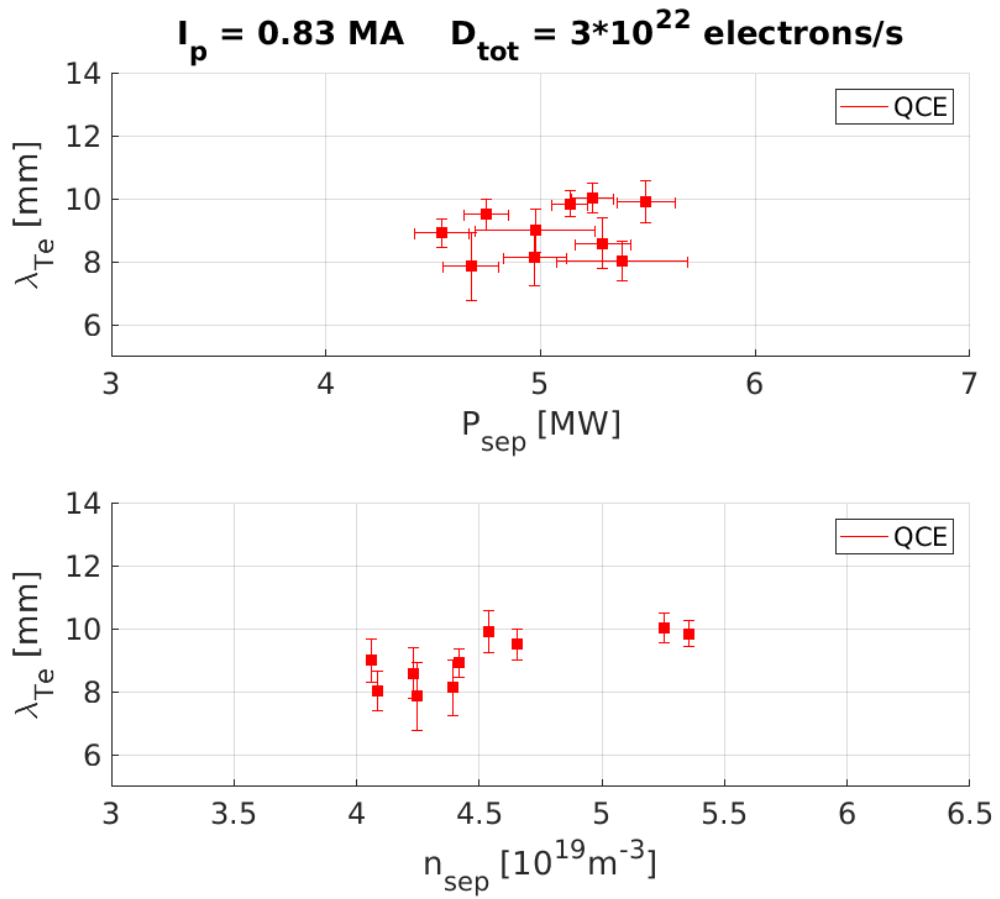


Figure 5.12: λ_{Te} vs. P_{sep} and n_{sep} for constant $I_p = 0.83 \text{ MA}$ and $D_{\text{tot}} = 3 \cdot 10^{22} \text{ electrons/s}$.

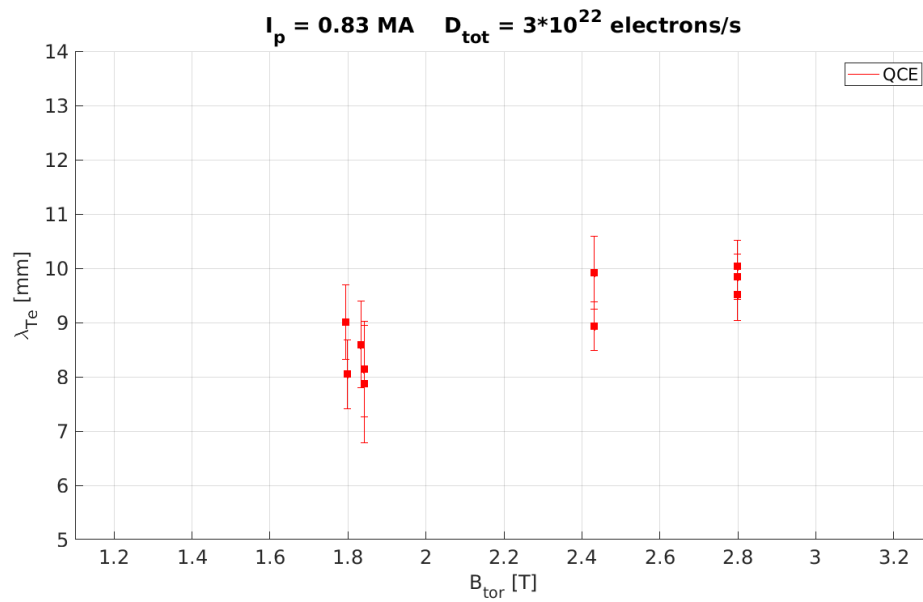


Figure 5.13: λ_{Te} vs. B_{tor} for constant $I_p = 0.83 \text{ MA}$ and $D_{\text{tot}} = 3 \cdot 10^{22} \text{ electrons/s}$.

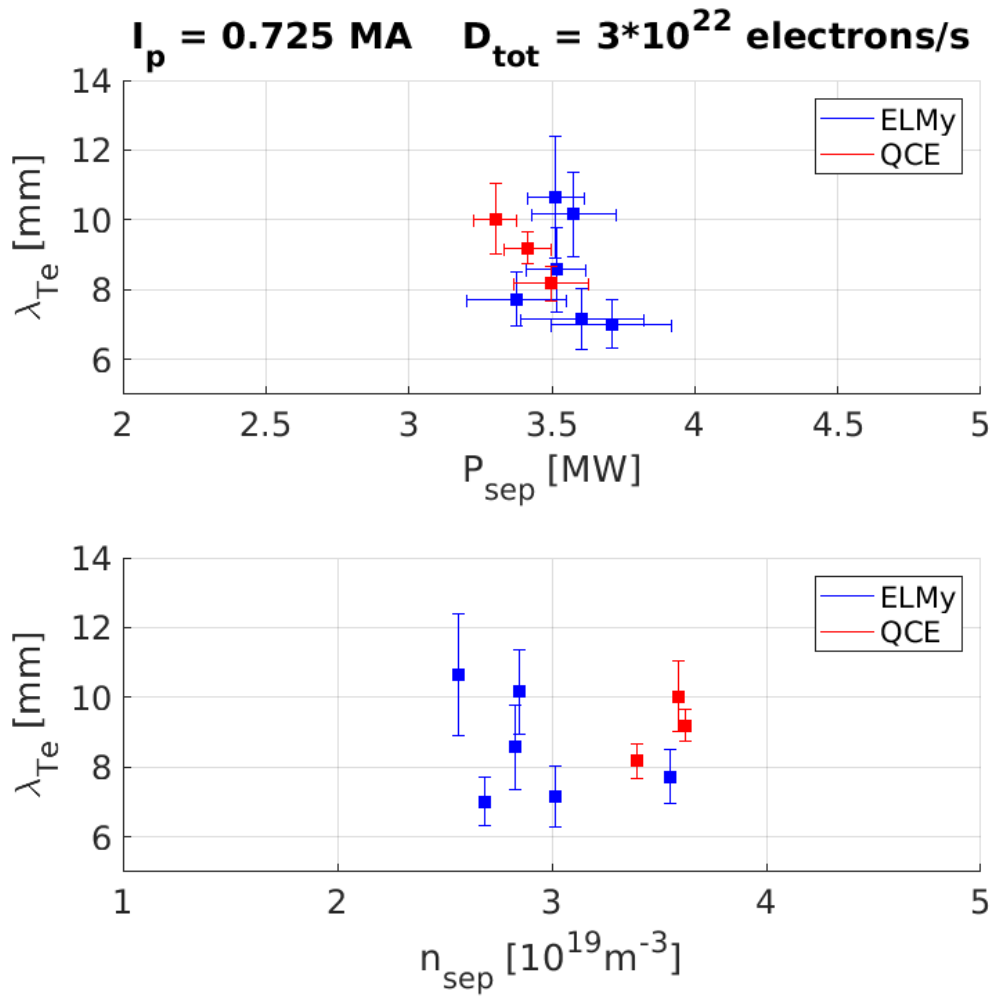


Figure 5.14: λ_{Te} vs. P_{sep} (only datapoints with P_{sep} in the range of 3 MW to 4 MW) and n_{sep} for constant $I_p = 0.725 \text{ MA}$ and $D_{\text{tot}} = 3 \cdot 10^{22} \text{ electrons/s}$.

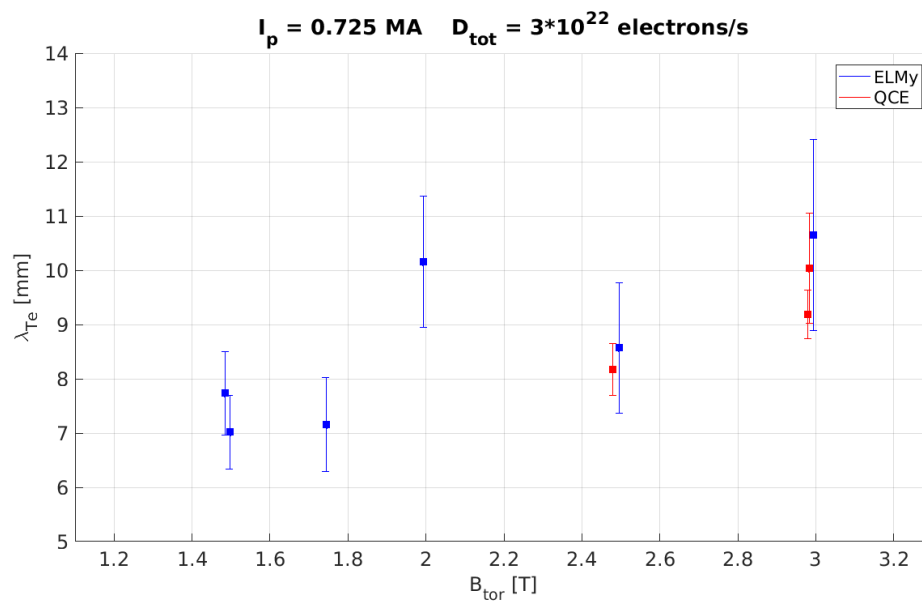


Figure 5.15: λ_{Te} vs. B_{tor} for constant $I_p = 0.725 \text{ MA}$ and $D_{\text{tot}} = 3 \cdot 10^{22} \text{ electrons/s}$ and P_{sep} between 3 MW and 4 MW.

5.4 λ_{Te} trends at constant q_{95}

The grouping for constant I_p in the last section showed the sign of the exponent of the B_{tor} dependency of λ_{Te} . Now the consideration of the group of discharges with constant $q_{95} = 4.5$ and $D_{tot} = 5 \cdot 10^{22}$ electrons/s will allow a comparison of the exponent of the B_{tor} dependency of λ_{Te} with the exponent of I_p . For this group n_{sep} and P_{sep} are again approximately constant, as shown in fig. 5.16. Now the only changing variables are I_p and B_{tor} . Since they are coupled by q_{95} through $q_{95} \propto \frac{B_{tor}}{I_p}$ and q_{95} is held constant, one receives the relation $B_{tor} \propto I_p$. This

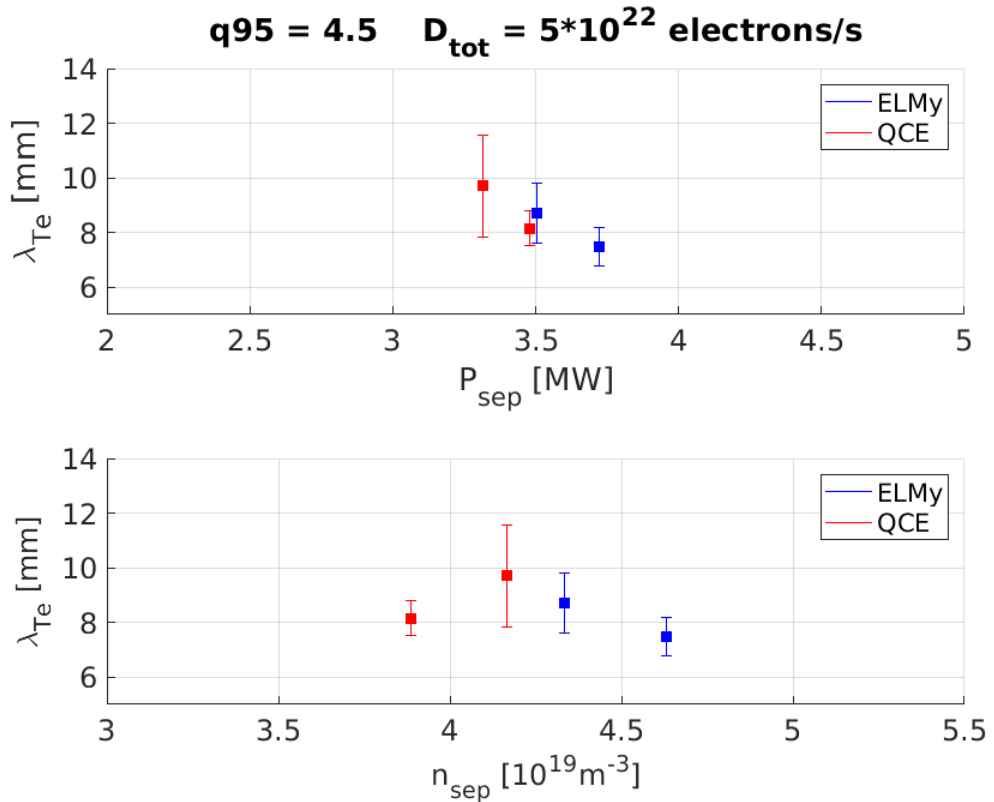


Figure 5.16: λ_{Te} vs. P_{sep} and n_{sep} for constant $q_{95} = 4.5$ and $D_{tot} = 5 \cdot 10^{22}$ electrons/s.

has a significant consequence for λ_{Te} and the dependency $\lambda_{Te} \propto B_{tor}^{\alpha} \cdot I_p^{\beta}$, where $\alpha > 0$ and $\beta < 0$, according to the theory in section 3.3 and the experiment in section 5.2, are the corresponding exponents that determine the dependency of λ_{Te} of these two variables. With $B_{tor} \propto I_p$ one obtains $\lambda_{Te} \propto B_{tor}^{\alpha+\beta}$ or equivalent

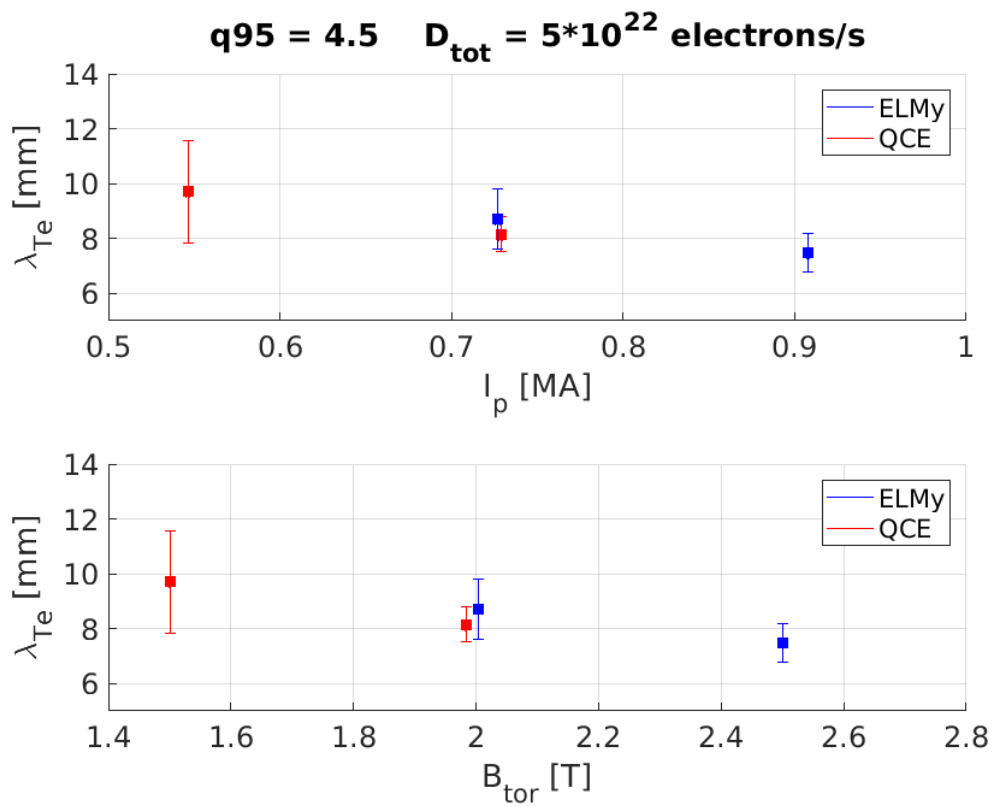


Figure 5.17: λ_{Te} vs. B_{tor} and I_p for constant $q_{95} = 4.5$ and $D_{\text{tot}} = 5 \cdot 10^{22}$ electrons/s

$\lambda_{Te} \propto I_p^{\alpha+\beta}$. Applying this to fig. 5.17 leads to the result that $\alpha + \beta < 0$, since λ_{Te} is falling with increasing B_{tor} or I_p . This allows, even without a non-linear-fit, the conclusion that λ_{Te} has a stronger dependency of I_p than of B_{tor} . The theoretical result in eq. (3.24) and the experimental result in eq. (5.4) confirm that.

6 Conclusion

In this final chapter the main results of this thesis are summed up.

The first and most important result is the comparison of the theoretical expected dependencies of λ_{Te} with the result of the non-linear-fit in fig. 5.11. The theoretical result, obtained in section 3.3, is:

$$\lambda_{Te} \propto n_{sep}^{\frac{7}{11}} \cdot P_{sep}^{-\frac{3}{11}} \cdot B_{tor}^{\frac{1}{11}} \cdot I_p^{-\frac{8}{11}} \quad (6.1)$$

and the outcome of the non-linear fit in section 5.2:

$$\lambda_{Te} = (3.39 \pm 0.37) \cdot B_{tor}^{0.24 \pm 0.06} \cdot I_p^{-0.79 \pm 0.12} \cdot P_{sep}^{0.2 \pm 0.04} \cdot n_{sep}^{0.2 \pm 0.06} \quad (6.2)$$

The comparison shows that the dependence of the I_p of both results agrees well, since the theoretical value is included in the errorbounds of the measured value. The B_{tor} dependency is in the experiment by the factor 3 larger than in theory, which is not justified by the errorbounds. A similar problem is found with the n_{sep} dependency, the theoretical value is by the factor 3 larger than the measured one and the errorbounds wouldn't allow such a big difference. Also the P_{sep} dependency doesn't match at all, even the sign is different.

In order to assess the quality of the result, it is compared with the corresponding result of T. Eich et al. in [5], where the n_{sep} dependency was not included:

$$\lambda_q \propto B_{tor}^{-0.8} \cdot q_{95}^{1.1} \cdot P_{sep}^{0.1} \quad (6.3)$$

T. Eich et al. investigated the dependencies of λ_q instead of λ_{Te} , but since $\lambda_q \propto \lambda_{Te}$ according to eq. (3.11), they have the same dependencies. For a better comparison it is convenient to insert $q_{95} \propto \frac{B_{tor}}{I_p}$. This leads to:

$$\lambda_q \propto B_{tor}^{0.3} \cdot I_p^{-1.1} \cdot P_{sep}^{0.1} \quad (6.4)$$

6 Conclusion

This leads to almost the same B_{tor} dependency, since their result is within the errorbounds of the one in eq. (6.2). The exponent of I_p differs by a factor of 1.4 and the one of P_{sep} is only half as big as the one in eq. (6.2). This comparison allows to see the result of this thesis in relation to another experimental result.

The minor results of this thesis are the clear observations in section 5.3 that λ_{Te} is increasing with increasing B_{tor} and in section 5.4 that the I_p dependency of λ_{Te} is higher than the dependency of B_{tor} .

Another result of this thesis is that SOL decay lengths do not show a correlation with the turbulence parameter α_{T} , while a clear correlation is found with n_{sep} .

Bibliography

- [1] D. Silvagni. *Experimental power exhaust studies of the improved confinement regime at the ASDEX Upgrade tokamak*. PhD thesis, Max Planck Institute for Plasma Physics, Max Planck Society; Feb. 2021. URL: <https://mediatum.ub.tum.de/doc/1595755/1595755.pdf>.
- [2] Sofía Aurora Díaz Esteban. *Investigation of the Structure of the Electron Temperature Profile around the Separatrix with the Thermal Helium Beam Diagnostic at ASDEX Upgrade (IPP 2021-13)*. Master thesis, Max Planck Institute for Plasma Physics, Max Planck Society; Sept. 2021. URL: https://pure.mpg.de/rest/items/item_3341548_1/component/file_3341551/content.
- [3] P. C. Stangeby. *The Plasma Boundary of Magnetic Fusion Devices*. University of Toronto Institute for Aerospace Studies, 2000. DOI: <https://doi.org/10.1201/9780367801489>.
- [4] G.F. Harrer. *On the origin and transport of small ELMs*. Dissertation, Technische Universität Wien, June 2020. URL: <https://doi.org/10.34726/hss.2020.44863>.
- [5] T. Eich et al. "Scaling of the tokamak near the scrape-off layer H-mode power width and implications for ITER". In: *Nuclear Fusion* 53.9 (2013), p. 093031. URL: <https://doi.org/10.1088/0029-5515/53/9/093031>.
- [6] H. J. Sun et al. "Study of near scrape-off layer (SOL) temperature and density gradient lengths with Thomson scattering". In: *Plasma Physics and Controlled Fusion* 57.12 (2015), p. 125011. DOI: 10.1088/0741-3335/57/12/125011.
- [7] D Silvagni et al. "Scrape-off layer (SOL) power width scaling and correlation between SOL and pedestal gradients across L, I and H-mode plasmas at ASDEX Upgrade". In: *Plasma Physics and Controlled Fusion* 62.4 (2020), p. 045015. URL: <https://doi.org/10.1088/1361-6587/ab74e8>.

- [8] T. Eich et al. "Turbulence driven widening of the near-SOL power width in AS-DEX Upgrade H-Mode discharges". In: *Nuclear Fusion* 60.5 (2020), p. 056016. DOI: 10.1088/1741-4326/ab7a66. URL: <https://doi.org/10.1088/1741-4326/ab7a66>.

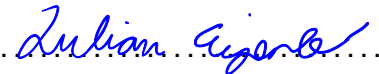
Name: Julian Eiperle

Matrikelnummer: 1052296

Erklärung

Ich erkläre, dass ich die Arbeit selbständig verfasst und keine anderen als die angegebenen Quellen und Hilfsmittel verwendet habe.

Ulm, den 07.06.2022



Julian Eiperle